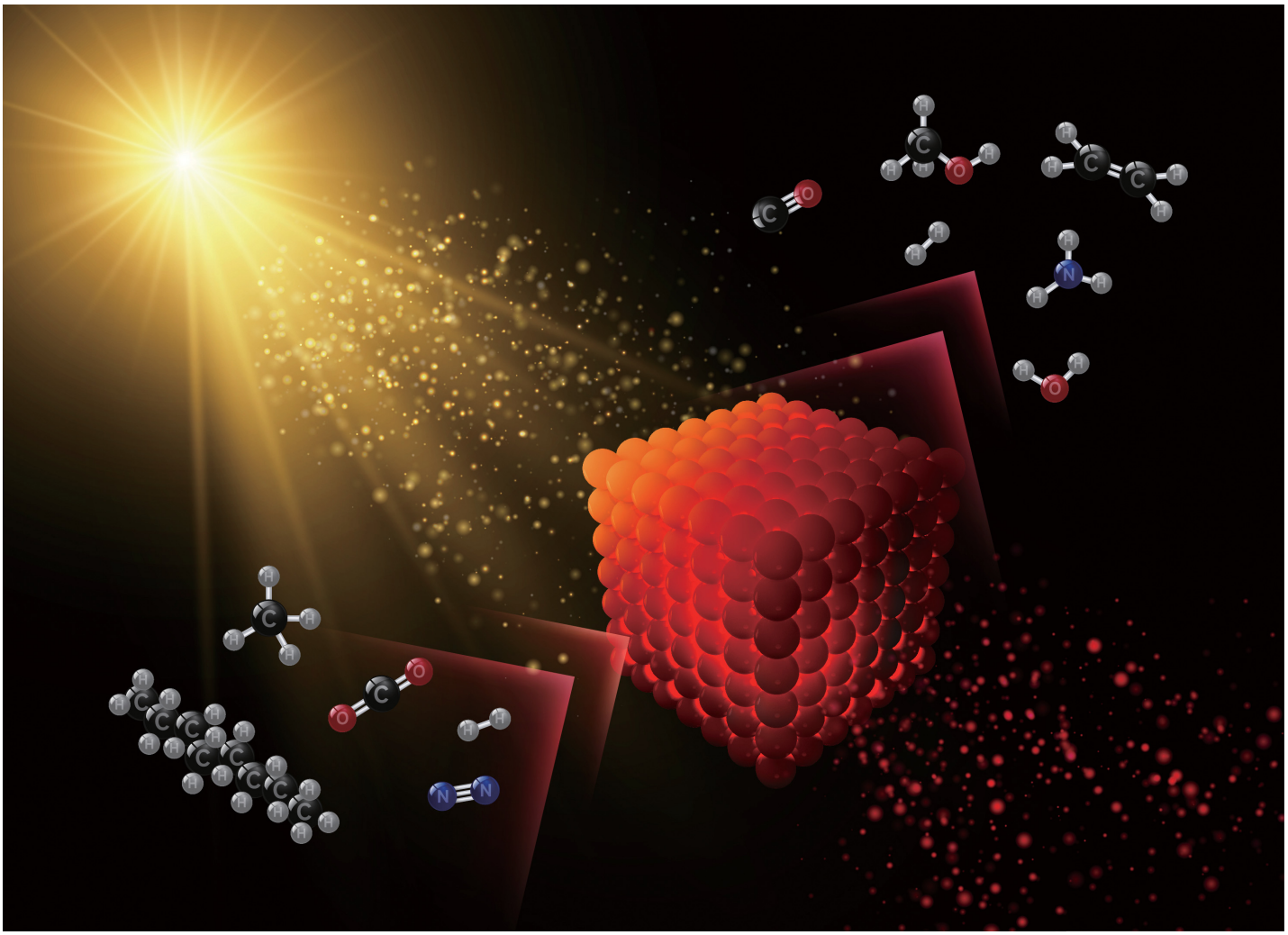

Showcasing research from Professor Wang's laboratory, School of Science and Engineering, The Chinese University of Hong Kong, Shenzhen, Shenzhen, Guangdong, China.

Photon and phonon powered photothermal catalysis

Photothermal catalysis has emerged as a groundbreaking approach to driving chemical reactions with photons and phonons. This method uniquely combines photonic and phononic elements of the light, offering enhanced reaction rates and tunable selectivity under moderate conditions. This work delves into the fundamental mechanisms of photothermal catalysis, focusing on the conversion processes and synergistic effect of photons and phonons, including key application advancements. The fundamental understanding of the role of photons and phonons could guide future investigations into mechanisms and application development of photothermal catalysis.

As featured in:

See Wenguang Tu, Lu Wang *et al.*, *Energy Environ. Sci.*, 2024, **17**, 4461.

ROYAL SOCIETY OF CHEMISTRY

rsc.li/ees

Registered charity number: 207890

Energy & Environmental Science

ROYAL SOCIETY OF CHEMISTRY

PERSPECTIVE

View Article Online
View Journal | View Issue

Cite this: *Energy Environ. Sci.*, 2024, **17**, 4461

Photon and phonon powered photothermal catalysis

Chang Xu,†[a] Qijun Tang,†[ab] Wenguang Tu*[a] and Lu Wang*[a]

Received 20th February 2024,
Accepted 30th April 2024

DOI: 10.1039/d4ee00783b

rsc.li/ees

Photo-thermal catalysis, leveraging light as an energy source, has emerged as a groundbreaking approach in driving chemical reactions. This method uniquely combines photonic and phononic elements of solar energy, offering enhanced reaction rates and altered selectivity under moderate conditions. This work delves into the core mechanisms of photo-thermal catalysis, focusing on the conversion processes and synergistic effect of photons and phonons, including the key advancements in applications such as catalytic CO_2 and CH_4 conversion, NH_3 synthesis, and plastic upcycling. A guideline for future investigations into mechanisms and application development of photothermal catalysis could be paved.

Broader context

By integrating traditional photocatalysis and thermocatalysis, photothermal catalysis has attracted significant attention from academia and industry. In a typical photothermal catalytic process, the photon represents the light, and the phonon represents the heat. Thus, the so-called photothermal catalysis can be driven either by phonons or photons and phonons. Unfortunately, the roles of photons and phonons in the photothermal catalytic process remain unclear due to the limited understanding of photothermal catalysis. In this perspective, we divide the recent advancement of photothermal catalysis into two distinct kinds, namely photon to phonon and photon and phonon, respectively, and provide an overview of the research from the viewpoint of photons and phonons. The reviewed work covers a wide range of reactions, including CO_2 hydrogenation, CH_4 conversion, NH_3 synthesis, and plastic upcycling. Such understanding could significantly contribute to unraveling the intricate mechanisms of photothermal catalysis from a fundamental physical chemistry perspective, thereby inspiring innovative design strategies for efficient photothermal catalysts in the future.

1. Introduction

Over the past few decades, a marked escalation in global energy demand has been observed, especially for the transportation and industrial sectors, in which the consumption of fossil fuels is dominated.[1] This reliance on fossil fuels has precipitated substantial pollution challenges, notably through the emission of greenhouse gases such as carbon dioxide (CO_2) and methane (CH_4).[2] Thus, a global strategic plan is to use renewable energy to replace traditional fossil fuels and eliminate the carbon footprint.[3] A diverse array of renewable energy options, including wind energy,[4] geothermal energy,[5] wave energy,[6] and solar energy,[7] have emerged and are increasingly gaining traction.

Solar energy, in particular, is considered a clean, plentiful, and perpetual energy resource. Utilization of solar energy has been extensively explored in areas such as photocatalysis,[8] photovoltaics,[9] and solar water heating.[10] Photocatalysis, a process to convert solar energy into chemical energy, has attracted considerable attention due to its mild reaction conditions and it is environmentally benign.[11] However, the efficiency of photocatalysis still falls short of practical application benchmarks. For instance, most photocatalysts are limited to absorbing ultraviolet light, which constitutes roughly 5% of the solar spectrum.[12] Additionally, the activation energy in photocatalysis is often insufficient to initiate reactions, especially when compared to traditional thermocatalysis, which typically operates under more extreme conditions (*e.g.*, high temperatures and pressures).

Addressing this challenge, photothermal catalysis has emerged as a novel paradigm. Photothermal catalysis involves the mutual conversion between photons and phonons, both of which play several roles during the reaction. The photons have to be absorbed by the catalyst, and then (1) excite the charge carriers to participate in the reaction or tune the acidity and basicity of the active sites, (2) excite the charge carriers to recombine and convert into phonons *via* thermalization, and (3) generate phonons *via* localized surface plasmon resonance

[a] *School of Science and Engineering, The Chinese University of Hong Kong, Shenzhen, 518172, Guangdong, P. R. China. E-mail: tuwenguang@cuhk.edu.cn, lwang@cuhk.edu.cn*
[b] *School of Chemistry and Materials Science, University of Science and Technology of China, 230026, Hefei, Anhui, P. R. China*
† C. X., and Q. T. contributed equally to this paper.

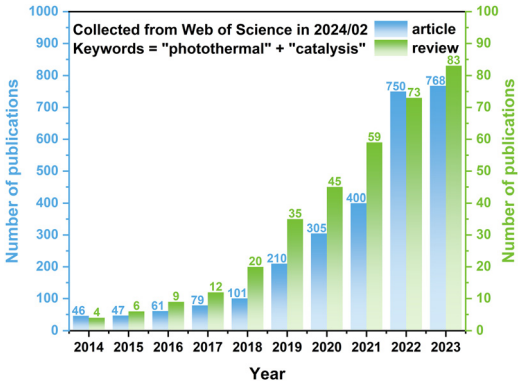

Fig. 1 Number of publications (articles and reviews) related to "photothermal" and "catalysis". The data were collected from the Web of Science in February 2024.

(LSPR).[13–15] The thermal energy of photothermal catalysis is an embodiment of phonons, which could be provided externally or converted from photons and decrease the reaction barrier by elevating the temperature.[16] Due to these advantages, photothermal catalysis is receiving increasing attention, as evidenced by a growing body of related research (refer to Fig. 1). Although some reviews have introduced photothermal catalysis *via* the simple classification of photothermal catalysis into photo-assisted thermocatalysis, thermal-assisted photocatalysis, and photothermal-synergistic catalysis,[14,17–20] it is necessary to provide one review to deeply understand the mechanisms of photothermal catalysis and highlight the recent advancements of photothermal catalysis.

This review will explore the mechanisms underlying photothermal catalysis, focusing on the conversion of photons to phonons and the synergistic interplay between them. It will then categorize and summarize applications of photothermal catalysis, including CO_2 and CH_4 conversion, NH_3 synthesis, and plastic upcycling. The review concludes with insights and future perspectives on photothermal catalysis, aiming to deepen understanding and foster further advancements in this field.

2. Mechanism of photothermal catalysis

Photothermal catalysts have garnered widespread application across a variety of catalytic domains, notably in CO_2 hydrogenation,[21] dry reforming of methane,[22] and NH_3 synthesis,[23] among others. The cornerstone of their broad utilization lies in the maximal energy conversion efficiency inherent in the photothermal process. This process adeptly converts electromagnetic energy into either heat or charge carriers with notable efficiency, both of which significantly influence catalytic activity. The operational mechanisms of photothermal catalysis can be broadly categorized into two distinct types, as illustrated in Fig. 2: photon → phonon and photon + phonon. It is critical to acknowledge that these two mechanisms often operate concurrently, albeit to varying extents, within a given photothermal catalytic process.[24]

2.1 Photon → Phonon

The term 'photon → phonon' encapsulates the process whereby electromagnetic energy is transmuted into thermal energy. This

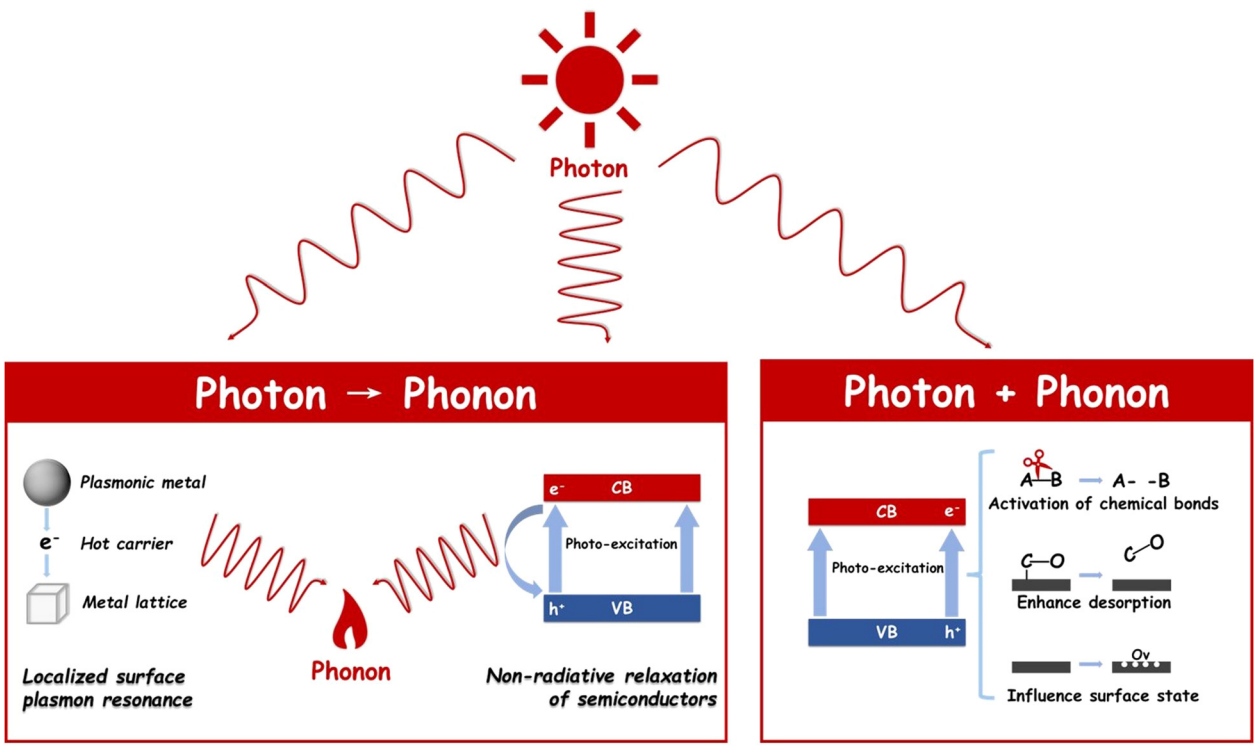

Fig. 2 Mechanism of photothermal catalysis including photons → phonons, and photons + phonons.

conversion can be efficiently facilitated through mechanisms such as the localized surface plasmon resonance (LSPR) effect or non-radiative relaxation in semiconductors. These processes underscore the interaction between light and matter in the realm of photothermal catalysis, offering an in-depth understanding of energy transformation at the nanoscale.

2.1.1 LSPR. Localized surface plasmon resonance (LSPR) is often observed in metal nanoparticles like Ag, Au, and Cu.[25,26] Under the influence of external light irradiation, an intriguing phenomenon occurs when the frequency of incident photons aligns with the natural oscillation frequency of surface conduction electrons in metallic nanoparticles.[27] This phenomenon, known as LSPR, arises from the collective oscillations of electrons at the nanoparticle surface. One of the characteristics of LSPR is the enhancement of the local electric field, a consequence of the incident electromagnetic wave and the resonant frequency of conduction electrons being in phase.[28]

Upon excitation, excited electrons undergo decay through either a radiative pathway, manifesting as re-emitted photons, or a non-radiative pathway, which involves electron–electron collisions and electron–hole pair recombination.[29] Notably, when plasmon energy is non-radiatively dissipated within the metallic nanoparticles—a process also referred to as 'Landau damping'[30]—energetic 'hot' charge carriers are generated within the plasmonic structure.[28] These carriers, if sufficiently energized, can escape the plasmonic nanoparticles, injecting into adjacent surface adsorbates or semiconductors, thereby triggering surface chemical reactions at a femtosecond (fs) scale.[31]

Alternatively, 'hot' electrons that do not contribute to surface reaction charge migration are transformed into metal lattice phonons *via* electron-lattice collisions, leading to a rise in metal lattice temperature at the picosecond (ps) level.[32] Subsequently, this thermal energy diffuses into the surrounding environment at the nanosecond (ns) level through phonon–phonon scattering.[33] This heat transfer, stemming from the photon-to-phonon conversion, not only facilitates mass transfer but also enhances reaction rates from a thermodynamic perspective.

In summary, LSPR encompasses three concurrent processes: the enhancement of the local electric field, the generation of energetic hot charge carriers, and a localized heating effect. Collectively, these mechanisms significantly boost the reaction rate.[34,35]

2.1.2 Non-radiative relaxation of semiconductors. Apart from the LSPR effect of metallic materials, semiconductors are capable of facilitating photon-to-phonon transformation through non-radiative relaxation. Within semiconductors, incident light possessing energy equal to or surpassing the band-gap energy can trigger the excitation of electrons from the valence band (VB) to the conduction band (CB), generating holes in the VB.[36] These electrons may revert to the base of the CB or back to the VB through either radiative means (emitting photons) or non-radiative means (releasing phonons). During non-radiative relaxation, electrons rapidly transition to lower energy states, emitting energy as lattice phonons, which ultimately raises the temperature of the semiconductor. Although the non-radiative relaxation in traditional photocatalysis is considered to be a detrimental factor, the external role in elevating the temperature could further improve the catalytic performance and quantum efficiency.

2.2 Photon + Phonon

As previously discussed, phonon (or heat) can come from the LSPR effect, non-radiative relaxation of semiconductors, and external heating. All sources of phonon (or heat) will synergistically contribute to the thermal catalytic process including providing the driving force for the reaction, lowering the activation energy, facilitating the breaking of chemical bonds, and enhancing the adsorption and desorption of reactants and intermediates.[37–39]

In photothermal catalysis, photons play pivotal roles not only in transforming themselves into phonons but also in influencing and altering the thermal catalysis process by modulating the surface properties of the catalyst or influencing the reaction pathway. For example, Ouyang's group used 2D black In_2O_{3-x} nanosheets for photothermal CO_2 reduction. The photo-induced oxygen vacancies not only enhanced light harvesting but also improved the chemical adsorption of CO_2 molecules. Therefore, both high activity (103.21 mmol g_{cat}^{-1} h^{-1}) and CO selectivity (nearly 100%) were achieved on In_2O_{3-x} nanosheets. A similar phenomenon was also discovered by Li's group that under light illumination, oxygen vacancies in CeO_2 are created by photo-induced electrons during dry reforming of methane (DRM), thereby replenishing the consumed oxygen and maintaining stable CO_2 thermo-activation.[40] Moreover, electron–hole pairs can induce alterations in the catalyst's surface state through the introduction of charged species (electrons and holes), redox reactions, or the creation of defects, indirectly impacting catalytic performance.[41] Time-dependent density functional theory (TDDFT) calculations and experimental characterization by Singh and colleagues demonstrated that the surface frustrated Lewis pairs (FLPs) on $In_2O_{3-x}(OH)_y$, constituted of a Lewis acid (coordinately unsaturated proximal In) and a Lewis base (InOH surface), were enhanced under light illumination.[13] This enhancement is corroborated by experimental findings showing a reduction of 21 kJ mol^{-1} in the activation energy of the Reverse Water Gas Shift Reaction (RWGS) in the presence of light.[42] Besides, in our recent research,[43] it was uncovered by experimental results and DFT calculations that the introduction of light would enable a new pathway of the RWGS reaction in a tandem ethane dehydrogenation and CO_2 hydrogenation system. As a result, the ethane dehydrogenation reaction was shifted with the rate of ethylene 11.5 mmol g^{-1} h^{-1} at 650 °C and the CO production rate increased to 5.5 mmol g^{-1} h^{-1} at 650 °C.

In a word, the combination of phonon and photon will provide a stronger driving force for the reaction, facilitate the breaking of chemical bonds, enhance the adsorption and desorption of reactants and intermediates as well as change the surface properties of catalysts, achieving synergistic enhancement of catalytic reactions through photo and thermal cooperation.

2.3 Other parameters

Due to the optimal exploitation of the photo-thermal effect in catalytic processes, the intense light absorption, efficient charge carrier generation, and high capacity for thermal energy production or transformation of photothermal catalysts should be considered as well.[24] Thus, the effect of the physicochemical properties of the materials and the corresponding temperature measurement methods will be introduced.

2.3.1 Size and morphology for plasmonic materials. In plasmonic materials, the phenomena of LSPR are critically dependent on the dimensional attributes and geometric configurations of the materials.[44,45] These characteristics not only significantly impact the efficiency of charge carrier generation but also profoundly influence the related thermal properties (thermal energy production or transformation) of the material.

In theory, the quantity of hot carriers is positively correlated with the size of plasmonic nanoparticles (NPs).[46] However, since the dissipation of most energy by scattering or heating, the energy of generated hot carriers is always close to the Fermi level state. In contrast, smaller NPs could generate fewer electron–hole pairs, with higher energy states and notably shorter lifetimes (on the order of femtoseconds).[47] The elevated energy of hot electrons increases the probability of populating acceptor states or overcoming Schottky barriers, which is paramount in photothermal catalysis. Nevertheless, a smaller NP size does not necessarily enhance overall photothermal performance. This diminution may result in inefficient charge carrier separation, attributed to spatial confinement.[48,49] On the other hand, increasing NP size could trigger a red shift in the resonant frequency of plasmonic NPs, facilitating a more efficient absorption of visible and IR regions.[49,50] In addition, the size could also influence the heating capability of plasmonic structures. The plasmon-heating effect in metallic nanospheres scales quadratically with the NP radius. However, larger plasmonic NPs tend to undergo radiative decay more readily, diminishing localized heat dissipation.[51] Consequently, achieving an optimal balance between these size-dependent effects is crucial in the design of plasmonic NP-based catalysts.

Morphology is another key parameter determining the optical properties of nanostructures. Bar shapes, bipyramids, or branched structures exhibiting a red shift in their primary localized LSPR absorption peaks are thus better suited for harnessing the low-energy regions of the solar spectrum.[52–54] In addition, the efficiency in hot carrier generation is also intimately related to the morphology. Geometries that foster strong, uneven electric fields and pronounced confinement effects can produce high-energy hot electrons and holes. Other geometries, such as thin films or nanosphere structures, are the opposite.[55,56] Moreover, the morphology also plays a pivotal role in determining heat production within plasmonic nanostructures.[57] Specifically, sharp, flat, or elongated geometries have been shown to facilitate more intense heat generation compared to spherical counterparts.[58] This underscores the importance of carefully considering nanostructure morphological aspects in designing and optimizing plasmonic materials for specific applications.

2.3.2 Morphology for hybrid materials. Hybrid structures represent a prevalent and straightforward approach to enhancing the performance of photothermal catalysis, typically comprising an inorganic host or support (most cases are metal oxides) functionalized with plasmonic or non-plasmonic metallic NPs. In such configurations, one or several elements may serve as the catalytically active sites.

Among them, metal/semiconductor hybrid materials have emerged as a particularly extensively researched system. An ideal semiconductor support for photothermal catalysts is characterized by high surface area and robust broadband optical absorption, which could facilitate the generation of charge carriers or elevate local temperatures. Typically, these structures incorporate narrow bandgap metal oxide semiconductors, which are rich in defects and possess mid-bandgap states, significantly enhancing light absorption in the low-energy regions.[24,34,59,60] For instance, the subsurface oxygen defects could electronically interact with active sites by embedding metallic In into In_2O_3 to enhance photothermal catalytic CO_2 reduction.[61] Under the effect of electron-delocalization of O–In–(O)V_o–In–In structural units at the interface, the electrons in the subsurface oxygen defects are extracted and accumulate at the active sites of the surface. This phenomenon enhances the electronic coupling with CO_2 and stabilizes the intermediate, increasing the turnover frequency of CO_2 reduction to 7615 h^{-1}.

In addition, materials with high porosity and high surface area (MOFs and zeolites) are a relatively underexplored avenue in photothermal catalysis, but are emerging as a promising field of research.[17,62,63] A pioneering study by Jiang's group introduced Pt/PCN-224(M) composites, which integrated Pt nanocrystals and porphyrinic MOFs, marking the first report of the photothermal effect in MOFs.[64] The transfer of hot electrons from Pt to PCN-224(M) leads to a decrease in electron density on the Pt surface. This dynamic can be finely adjusted to optimize catalytic performance by carefully balancing the influences of the Schottky junction and plasmonic effects through modulation of light intensity. This synergistic mechanism improves the overall photocatalytic performance, surpassing the individual contributions from each component.

Core–shell structured hybrid materials capitalize on their bifunctional nature to offer tunable optical, electronic, and thermal properties, presenting a compelling approach for the development of materials with enhanced photothermal performance.[64] A notable example is the work of Kumar's group, which developed Pt@TiO_2–AuNPs catalysts.[65] Au plasmonic nanoparticles (NPs) have been enveloped in a TiO_2 coating with Pt NPs to form a core–shell structure. Compared to bare Au NPs, the inclusion of a thin TiO_2 layer leads to an increased quantum yield, attributable to an expansion in surface area, a red-shift and broadening of the LSPR peak, and an augmented light absorption capability. Furthermore, the strategic placement of Pt NPs plays a crucial role in capturing hot electrons from the CB of TiO_2, effectively restraining electron–hole recombination and thereby enhancing the overall reaction rate.

2.4 Temperature measurement method

Accurate temperature measurement of photothermal catalysis is crucial for distinguishing between thermal and non-thermal contributions to the overall process. Here, some common temperature measurement methods have been overviewed.

(i) Directly measuring the temperature of bulk catalysts using a thermocouple in real-time.

(ii) IR thermography grounded in the Planck blackbody emission principle, could estimate the local temperature by the emitted energy of a body.[17]

(iii) Tip-enhanced Raman spectroscopy (TERS) enables mapping local temperatures at the nanometer scale by calculating the ratio of anti-Stokes and Stokes Raman signal intensities.[66,67] Ozin's group has probed the precision local temperature of $Pd@Nb_2O_5$ by exploring Stokes and anti-Stokes Raman bands, as high as 470 °C.[68]

(iv) Arrhenius plots are a fundamental tool for assessing the impact of temperature on chemical reaction rates, which exists as a crucial parameter, activation energy (E_a). Utilizing this principle, our group investigated the mechanistic pathways driving the photothermal catalysis reaction.[34] Comparing activation barriers under both light and dark conditions at consistent temperatures, it is possible to determine the impact of photon-induced charge carriers on the reaction rates. In the case of the RWGS reaction, the Arrhenius plot revealed two nearly parallel lines for dark and light. The similar activation energies imply the same reaction mechanism, indicating that solar energy was mainly converted into thermal energy (Photon → Phonon) to enhance the catalytic performance.

(v) Based on the equilibrium constants to calculate the local temperature of catalysts. Due to the localized nature of heat generation, a significant temperature gradient exists between the catalyst and its surroundings. He's group calculated the local temperature of Ni catalysts based on the equilibrium constants and constituent content of different product gases when photothermal CO_2 hydrogenation reactions reached the equilibrium state.[69]

(vi) The measured temperature may require infrared calibration. Take the core–shell structured Ni@p-SiO_2 catalyst of He's group as an example.[69] Compare the FTIR spectrum of the SiO_2 shell and theoretical spectra of the blackbody radiation, revealing that the SiO_2 shell could absorb the infrared light radiated from the Ni (the heat source). However, the calculated contribution of thermal radiation to the total heat dissipation of Ni NPs over this reaction could reach up to 43%, indicating that the measured local temperature should be increased by 60 K.

3. Photothermal catalysis for reaction systems

In conventional photocatalytic processes, the infrared region, which constitutes approximately 43% of solar radiation's total energy, is often overlooked due to it having insufficient energy to facilitate electronic transitions in most semiconductors. However, there are significant photothermal conversion effects in some suitable narrow-band semiconductor materials or some specific metals. In the context of metallic substances, this conversion is attributed to the relaxation of intense electric fields generated by local surface plasmon resonance under illumination. This phenomenon not only induces localized elevated temperatures but also generates high-energy 'hot electrons'. Conversely, in semiconductor materials, analogous conversion processes are driven by either Auger recombination or Shockley–Reed–Hall mechanisms, wherein surplus energy is transformed into thermal energy *via* phonon vibrations.[24]

With the further exploration and advancement of photothermal effects, photothermal catalysis as an emerging catalytic paradigm has been proposed, promising enhanced utilization of renewable solar energy. This innovative approach involves the integration of photocatalysis and thermocatalysis, harnessing both photo- and thermo-effects in a unified catalytic system. This integration facilitates the conversion of solar energy into thermal and chemical forms.[70] To date, photothermal catalysis has been applied in various reactions with different internal mechanisms ("photon → phonon" and "photon + phonon"), as shown in Tables 1 and 2.

3.1 CO_2 hydrogenation

The escalating concentration of atmospheric CO_2 (surpassing 420 ppm) represents a critical challenge for human sustainability.[71] To overcome this issue, substantial research efforts have been devoted to converting CO_2 into fuel *via* solar-related catalytic technologies. Among these, photothermal catalysis shows considerable potential in facilitating CO_2 conversion under relatively mild conditions.

Since the seminal report in 2014,[72,73] photothermal hydrogenation of CO_2 has emerged as a vibrant and rapidly growing field of research. This approach has demonstrated its versatility across a spectrum of applications, including but not limited to the reverse water gas shift (RWGS) reaction,[59,74,75] methanol synthesis,[34,76–78] the Sabatier reaction,[69,79–81] and the production of C_{2+} compounds.[82–84] Each of these applications showcases the adaptability of photothermal technology and underscores its significance in addressing the global CO_2 challenge.

Photon → Phonon. Pristine In_2O_3, characterized by its pale-yellow color and abundant oxygen vacancies, has been recognized for its efficacy in promoting adsorption and activation during thermochemical CO_2 hydrogenation, serving as a quintessential thermal catalyst.[85] Nevertheless, its relatively large band gap of 2.8 eV, primarily absorbing ultraviolet light, limits its efficiency as a photothermal CO_2 hydrogenation catalyst.[86] A significant breakthrough was achieved by Ozin, who demonstrated that stoichiometric In_2O_3 could be transformed into an oxygen-deficient, non-stoichiometric form (In_2O_{3-x}/In_2O_3) *via* thermal hydrogenation at 400 °C, as illustrated in Fig. 3(A) and (B).[59] This transformation not only alters the color of materials to black but also markedly enhances its activity and selectivity for both photothermal and photochemical CO_2 hydrogenation. Impressively, under ambient conditions, In_2O_{3-x}/In_2O_3 achieved a CO yield of 1874.62 μmol h^{-1} m^{-2} with 100% selectivity,

Table 1 Performance comparison of reference photothermal catalysts (Photons → Phonons)

Catalysts	Catalytic performance	Reaction conditions	Ref.
$Cu_2ZnAl_{0.5}Ce_5Zr_{0.5}O_x$	CO: 248.5 mmol g^{-1} h^{-1}	Flow reactor, CO_2/H_2 ratio = 1 : 1, (459 °C) 40 mL min^{-1}, simulate solar light source, ~2 suns	88
$H_zIn_2O_{3-x}(OH)_y$	CO: 433.68 μmol g^{-1} h^{-1} CH_3OH: 23.03 μmol g^{-1} h^-	Flow reactor, CO_2/H_2 ratio = 1 : 1, (300 °C) 4 mL min^{-1}, 300 W Xe lamp, ~6 suns	34
$0.35Ru@Ni_2V_2O_7$	CO_2 conversion: 93.5%, CH_4: 114.9 mmol g^{-1} h^{-1}	Batch reactor, pressure: 1 bar, (350 °C), 0.5 h CO_2/H_2 ratio = 1 : 4, 300 W Xe lamp, 2.0 W cm^{-2}	79
Ni@p-SiO_2-30	CO_2 conversion: 54%, CO selectivity: 83%, CH_4: 20.6 mol g^{-1} h^{-1}	Batch reactor, pressure: 1 bar, (579 °C), 1 h CO_2/H_2 ratio = 1 : 1, 300 W Xe lamp, 2.8 W cm^{-2}	69
CoFe-650 alloy/Al_2O_3	CO_2 conversion: 78.6%, CO selectivity: 4.97%, CH_4 selectivity: 59.77%, C_{2+} selectivity: 35.26%	Batch reactor, pressure: 1.8 bar, CO_2/H_2 ratio = 1 : 4, 300 W Xe lamp, 5.2 W cm^{-2} (320 °C), 2 h	91
hm-Ni/Al_2O_3	CO: 9614.3 mmolg_{Ni}^{-1} min^{-1} H_2: 8573.0 mmol g_{Ni}^{-1} min^{-1}	Flow reactor, 89.5 mL min^{-1}, $CH_4/CO_2/N_2$ ratio = 3 : 3 : 4, 500 W Xe lamp, 345.6 kW cm^{-2}, 706 °C	107
Rh/$LaNiO_3$	CO: 527.6 mmol h^{-1} g_{Rh}^{-1} H_2: 452.3 mmol h^{-1} g_{Rh}^{-1}	Flow reactor, 50 mL min^{-1}, CH_4/CO_2/Ar ratio = 1 : 1 : 3, 300 W Xe lamp, 3.5 W cm^{-2}, 440 °C	108
Rh/$SrTiO_3$	CO: 4.5 μmol min^{-1} H_2: 4.4 μmol min^{-1}	Flow reactor, 10 mL min^{-1}, CH_4/CO_2/Ar ratio = 1 : 1 : 98, 50 W Hg–Xe lamp	109
Cu-CNN/Pd-BDCNN	CO: 852.6 μmol g^{-1} h^{-1} H_2: 844.1 μmol g^{-1} h^{-1}	Flow reactor, 10 mL min^{-1}, CH_4/CO_2/Ar ratio = 1 : 1 : 8, 300 W Xe lamp, 300 mW cm^{-2}	110
$AuRu_{0.31}$	NH_3: 101.4 μmol g^{-1} h^{-1}	N_2 pressure: 2 bar, water, 300 W Xe lamp, 400 mW cm^{-2}	118
Au@Ui0-66 powder	NH_3: 10.81 mmol g^{-1} h^{-1}	N_2, water (K_2SO_4), 300 W Xe lamp, 400 mW cm^{-2}	119
$Cu_{96}Fe_4$	NH_3: 1342 μmol g^{-1} h^{-1}	N_2, water, 300 W Xe lamp, 250 mW cm^{-2}	120
MoO_{3-x}	AQE: 1.24% (808 nm) SACE: 0.057%	N_2, water, 300 W Xe lamp,	121
AgNP-Co	Δ stress at break: 2.5 Mpa	LDPE, blue light (270 mW cm^{-2}), 55 °C, 120 h	129
AgNPs	Δ stress at break: 16 Mpa	PECA, 300 W Xe lamp, 600 mW cm^{-2} (445 nm), 140 °C, 1 h	130
CNT-PDA	PET conversion: 100% BHET yield: 30.69%	PET, Uv light 300 W, 600 mW cm^{-2}, 180 °C, 2 h, m_{PET}: 5 g,	131
Co SSCs	PET conversion: 100% BHET yield: 82.6%	PET, simulated sunlight, 0.74 W cm^{-2}, 180 °C, 3 h, m_{PET}: 0.5 g	132

surpassing the performance of all previously reported indium-oxide-based catalysts, as shown in Fig. 3(C). The introduction of oxygen vacancies in In_2O_{3-x}, along with unsaturated In and O sites, creates defect states within the band gap.[87] These defect states, situated near the conduction band (CB) and valence band (VB), are populated with charge-balancing electrons, enabling absorption over a broad solar wavelength range. This feature facilitates the separation of photogenerated charge carriers at the interface between In_2O_3 and In_2O_{3-x}, effectively driving CO_2 conversion through photothermal mechanisms. Furthermore, Ye's group has innovatively applied the high-entropy principle to modify the structure of Cu-based nanocatalysts.[88] By developing a polyvinylpyrrolidone (PVP) template technique, they synthesized a composite of six different elements, culminating in the creation of high-entropy 2D materials, $Cu_2ZnAl_{0.5}Ce_5Zr_{0.5}O_x$. Utilizing this highly entropic structure in CO_2 photothermal hydrogenation resulted in a photochemical energy conversion efficiency of 36.2% and a CO production rate of 248.5 mmol g^{-1} h^{-1}. This advanced material design approach markedly enhanced both catalytic stability and activity, promising to revolutionize the field of photothermal catalysis and pave the way for its industrial application.

Wang's group recently made a significant breakthrough by developing a new black indium oxide tandem catalyst for photothermal CO_2 conversion to methanol.[34] This novel catalyst, benefiting from surface site engineering, exhibits enhanced absorbance and concentration of surface [O], thereby overcoming the thermodynamic limitations typically associated with conventional methanol synthesis. This catalyst operates on a tandem reaction scheme, wherein CO, a by-product from the Reverse Water Gas Shift (RWGS) reaction, is utilized as an *in situ* feedstock for methanol formation. This tandem process transforms the traditionally competing RWGS and methanol synthesis into a cohesive reaction pathway within a flow reactor system. Under sunlight illumination, methanol selectivity of up to 33.24% and 49.23% at low (50%) and high (75%) hydrogen concentrations, respectively, was achieved. This development signals a promising advance towards the realization of a solar refinery for sustainable methanol production.

In the context of photothermal CO_2 methanation, ruthenium (Ru) catalysts are widely acknowledged for their efficacy, as evidenced by recent studies.[89] However, the scarcity and high cost of Ru have spurred the search for alternative catalysts that either minimize or eliminate the use of noble metals.[90] In this vein, Zou's group developed a $Ru@Ni_2V_2O_7$ catalyst, demonstrating remarkable methanation efficiency.[79] This catalyst operates *via* a synergistic mechanism between Ru and $Ni_2V_2O_7$, as shown in Fig. 3(D) and (E). Here, Ru clusters act as 'nano-heaters,' enhancing local thermal conditions (photon → phonon), which facilitate H_2 activation and H_2O desorption. The hydrogen atoms generated interact with CO_2 on the oxygen-vacancy-rich surface of $Ni_2V_2O_7$, leading to efficient CO_2 methanation. The $Ru@Ni_2V_2O_7$ catalyst achieves a CO_2 conversion efficiency of 3.5%, approaching the thermodynamic

Table 2 Performance comparison of reference photothermal catalysts (Photon + Phonon)

Catalysts	Catalytic performance	Reaction conditions	Ref.
$10Cu5Ga/CeO_2$	CO: 111.2 mmol g^{-1} h^{-1}	Flow reactor, CO_2/H_2 ratio = 1 : 1, 20 mL min^{-1}, 300 W Xe lamp, 1.95 W cm^{-2}, 320 °C	63
$ZnFe_2O_4$	CH_3OH: 1757 μmol g^{-1} h^{-1}	Flow reactor, 6.5 bar, CO_2/H_2 ratio = 1 : 3, 8 mL min^{-1}, with external heat, LED white light, 1.83 W cm^{-2}, 254 °C	76
Ni–Ru/HZSM-5	CH_4: 6.76 mmol g^{-1} h^{-1}	Flow reactor, CO_2/H_2 ratio = 1 : 4, 5 mL min^{-1}, with external heat, 130 W Xe lamp, 3.5 W cm^{-2}, 300 °C	62
$CoFe_2O_4$	CO_2 conversion: 12.9% C_{2+}: 1.1 mmol g^{-1} h^{-1} C_{2+} selectivity: 29.8%	Flow reactor, CO_2/H_2 ratio = 1 : 4, 2.5 mL min^{-1}, with external heat, 300 W Xe lamp, 2 W cm^{-2}, 300 °C	92
Ni_3Fe_1	CO: 0.63 mol g^{-1} h^{-1} H_2: 0.33 mol g^{-1} h^{-1}	Flow reactor, 1.8 bar, 75 mL min^{-1}, CH_4/CO_2/Ar ratio = 1 : 1 : 2, 500 W Xe lamp, 3.62 W cm^{-2}, 350 °C	111
Ni–CeO_2–$CePO_4$	CO: 4 mmol g^{-1} h^{-1} H_2: 4 mmol g^{-1} h^{-1}	Flow reactor, 10 mL min^{-1}, CH_4/CO_2/Ar ratio = 1 : 1 : 2, four Prizmatix LEDs, (UV, blue, green, red and a beam combiner) 48.1 kW cm^{-2}, 350 °C	112
Pt/TiO_2	CO: 1499.2 mmol g^{-1} h^{-1} H_2: 1107.1 mmol g^{-1} h^{-1}	Flow reactor, 20 mL min^{-1}, CH_4/CO_2/Ar ratio = 48 : 48 : 4, with external heat, 300 W Xe lamp, 5 W cm^{-2}, 700 °C	113
Ni/Ga_2O_3	CO: ~200 μmol g^{-1} h^{-1} H_2: ~188 μmol g^{-1} h^{-1}	Flow reactor, 10 mL min^{-1}, CH_4/CO_2/Ar ratio = 1 : 1 : 4, with external heat, 300 W Xe lamp, 2.7 W cm^{-2}, 391 °C	114
Ni/TiO_2	NH_3: 55.7 μg g^{-1} h^{-1}	Flow reactor, N_2/H_2 = 1 : 3, 30 mL min^{-1}, with external heat, 300 W Xe lamp, 400 °C	120
Ru–Cs/MgO	NH_3: 4464 μmol g^{-1} h^{-1}	Flow reactor, N_2/H_2 = 1 : 3, 75 mL min^{-1}, with external heat, blue LED, 4.7 W cm^{-2}, 333 °C	121
$Cs_{10}Ru_2$@ST	NH_3: 3580 μmol g^{-1} h^{-1}	Flow reactor, N_2/H_2 = 1 : 3, 40 mL min^{-1}, with external heat, 300 W Xe lamp, 1 sun, 350 °C	122
Ru/C	NH_3: 1750 μmol g^{-1} h^{-1}	Flow reactor, N_2/H_2 = 1 : 3, 40 mL min^{-1}, with external heat, 300 W Xe lamp, 5.0 W cm^{-2}, 350 °C	123
g-C_3N_4	PS conversion: 100%, benzaldehyde selectivity: 51%, acetophenone selectivity: 31%, benzoic acid selectivity: 18%	PS, flow reactor, WHSV = 0.9 h^{-1}, 30 mL acetonitrile, 10 bar O_2, 300 W Xe lamp, 120 °C, 8 h, m_{PS}: 500 mg	134
DEG-ligated TiO_2	PET conversion: 100% BHET yield: 85%	PET, batch reactor, 30 mL CH_3CN, 10 bar O_2, simulated sunlight, 0.65 W cm^{-2}, 190 °C, 0.5 h, m_{PET}: 500 mg	135
Ni–Ti–Al	Hydrogen production: 34 mol kg^{-1} Jet fuel selectivity: 80%	LDPE, batch reactor, inert atmosphere N_2 simulated sunlight, 500 °C	136
Ru/TiO_2	LDPE conversion: 100%, C_5–C_{21} selectivity: 86%	LDPE, batch reactor, N_2/H_2 = 3 : 7, 30 bar Xe lamp, 3.00 W cm^{-2}, 220 °C, 3 h, m_{LDPE}: 80 mg	137

equilibrium limit for thermo-catalytic CO_2 methanation. Furthermore, drawing inspiration from the greenhouse effect, He and Ozin reported a nickel nanocrystal encapsulated in nano-porous silica (Ni@p-SiO_2).[69] This configuration enables heating of the nickel core through non-radiative relaxation of photogenerated electrons. The insulation and infrared shielding of the silica sheath yield a supra-photothermal effect, safeguarding the Ni core against sintering and coking. This design has led to industrially relevant rates of conversion, selectivity, and durability.

In 2018, Zhang's group introduced an innovative approach by employing CoFe alloy catalysts for photothermal CO_2 hydrogenation to hydrocarbons.[91] These catalysts, comprising CoFe alloys supported on alumina derived from layered double hydroxide nanosheets, exhibited high efficiency in the process. A critical aspect of their methodology involved modulating the reduction temperature between 300 °C and 700 °C, as shown in Fig. 3(G). This modification in reduction temperature allowed precise control over the CoFe-*x* surface chemistry, shifting product selectivity from CO to CH_4, and ultimately to C_{2+} hydrocarbons. Notably, the CoFe-650 catalyst, characterized by discrete alloy nanoparticles, demonstrated significant C–C coupling selectivity in CO_2 hydrogenation. As depicted in Fig. 3(H) and (I), under Xe lamp irradiation, the C_{2+} selectivity reached an impressive 35%, with an overall conversion rate of 78.6%. This represents a pioneering achievement in the field, marking the first report of such a high yield in C_{2+} hydrocarbon synthesis *via* photothermal CO_2 hydrogenation.

Photon + Phonon. The synergistic interaction of photon and phonon has been shown to enhance CO production in photothermal reactions. Ye's group reported a notable advancement with a high dispersity Ga–Cu/CeO_2 catalyst, synthesized using a Metal–Organic Framework (MOF)-assisted method.[63] This catalyst achieved a CO production rate of 111.2 mmol g^{-1} h^{-1} at 320 °C in photo thermal catalysis for CO_2 reduction, as depicted in Fig. 4(A) and (B). Then excluding the influence of the photothermal effect (photon → phonon) caused by IR light, the CO production under UV-vis light irradiation could also reach 54.8 mmol g^{-1} h^{-1}. This rate is about 1.6 times higher than that observed under dark conditions, highlighting the substantial enhancement of UV-vis light irradiation on activity *via* light-induced hot carriers. The mechanism underpinning this photothermal reaction suggests that the synergy effect of photon and phonon effectively reduces the apparent activation energy, thereby dramatically increasing CO production.

Additionally, Ozin's group explored zinc iron oxide spinel as a model photothermal catalyst, proposing an alternative strategy for methanol synthesis.[76] Though introducing photon energy could shift the reaction pathway to a new photothermodynamic excited equilibrium state (photon + phonon),

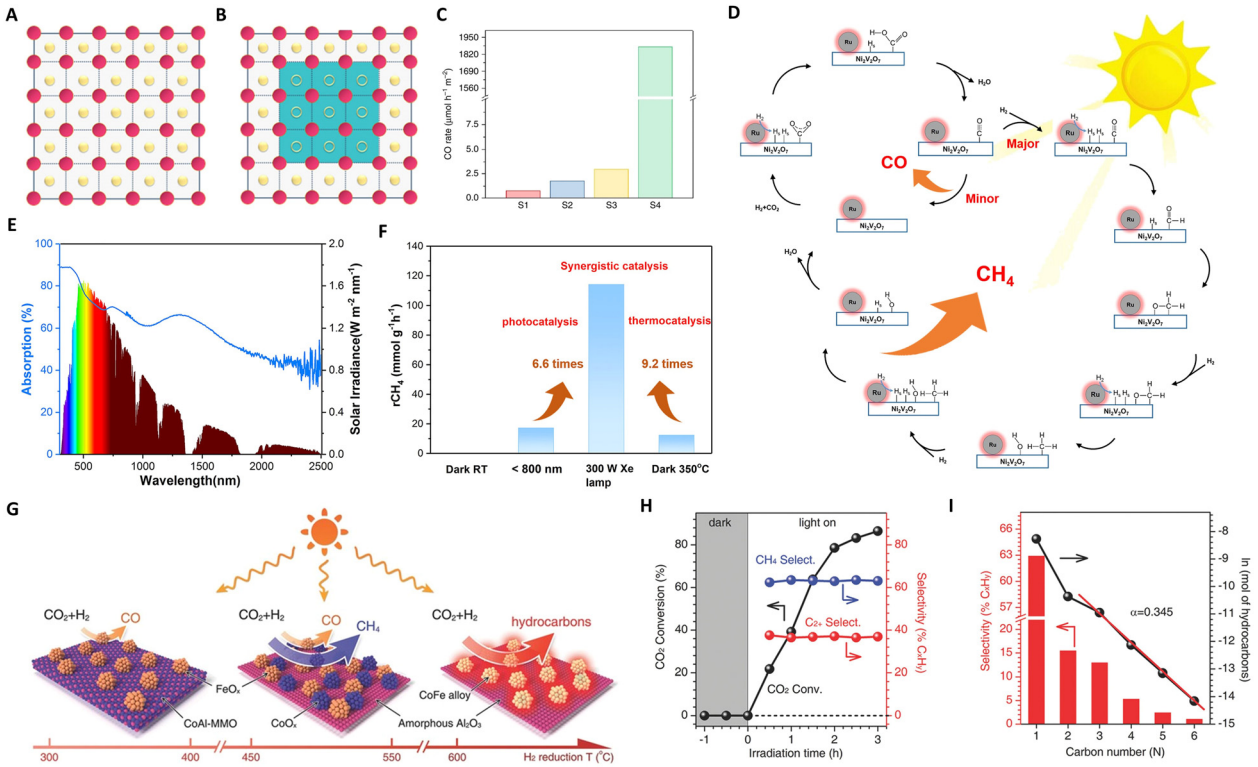

Fig. 3 (A) and (B) Graphical representation of the original and treated In_2O_3, wherein the blue region, pink dots, yellow dots, and yellow circles represent the amorphous phase, In atoms, O atoms, and [O], respectively. The scale bars are the same for all images, and green squares indicate the formation of an amorphous phase. (C) Photocatalytic evaluation of black indium oxide. These figures have been reproduced from ref. 59 with permission from Springer Nature, copyright 2020. (D) The proposed catalytic reaction mechanism for the Ru@NVO catalyst. (E) UV-vis-IR absorption spectrum of the NVO film. (F) Average CH_4 production rates over Ru@NVO at room temperature under the different conditions. These figures have been reproduced from ref. 79 with permission from Elsevier, copyright 2021. (G) Illustration of the different CoFe-*x* catalysts formed by hydrogen reduction of a CoFeAl-LDH nanosheet precursor at different temperatures. (H) The time course of CO_2 conversion and product selectivity for CO_2 hydrogenation over CoFe-650 under UV-vis irradiation. (I) The hydrocarbon product distribution obtained over CoFe-650 under UV-vis irradiation for 2 h. These figures have been reproduced from ref. 91 with permission from John Wiley & Sons, copyright 2017.

breaking the limitations of traditional thermodynamic equilibrium. Surface oxygen vacancies of $ZnFe_2O_4$ are crucial for trapping and concentrating photoinduced charge carriers as well as for CO_2 capture and activation at the same sites. This is because the reaction process primarily yields CO and methanol, both deriving from a common intermediate: bidentate carbonate anchored at oxygen vacancy sites. Thus, $ZnFe_2O_4$ could facilitate the transformation of feed gas through excited state intermediates, circumventing thermodynamic equilibrium constraints (photon effect) to improve methanol selectivity and yield, as shown in Fig. 4(C) and (D). By fine-tuning photon energy, approximately 80% of the photo-induced charge carriers participate in the chemical reaction before recombination, achieving a 17.5 times increase in methanol production rate to 1757.1 μmol g^{-1} h^{-1}.

In a recent study, Ozin *et al.* introduced a composite material comprising bimetallic nickel–ruthenium nanoparticles supported on protonated zeolite (Ni–Ru/HZSM-5).[62] The black Ni nanoparticles generate local heating effects, endowing Ni–Ru/HZSM-5 with exceptional light-harvesting capabilities. The bimetallic Ni–Ru nanoparticles, with a photothermal Ni core and Ru corona, provide the necessary thermal energy to enhance synergistic photothermal and hydrogen atom transfer effects, as illustrated in Fig. 4(E). The efficiency of this photothermal process was demonstrated in the CO_2 methanation reaction, comparing CH_4 formation rates under identical temperatures with and without light illumination. Under purely thermal conditions, the CH_4 formation rate was 1.88 mmol g^{-1} h^{-1}. However, under a 24 h light illumination reaction, this rate increased to 6.76 mmol g^{-1} h^{-1}, while maintaining a CH_4 selectivity of 89.4%. These results offer critical insights into the impact of photothermal heating and enable a high selectivity associative CO_2 methanation reaction pathway.

Furthering their contributions, Ozin's group developed a CoFe–$CoFe_2O_4$ alloy spinel nanocomposite for CO_2 hydrogenation under atmospheric pressure, as shown in Fig. 4(F).[92] In this system, the $CoFe_2O_4$ spinel is instrumental in facilitating the RWGS reaction, converting feed gas into CO, which then serves as a synthon for Fischer–Tropsch Synthesis (FTS) over the CoFe alloy. This results in a high C_2–C_4 rate and selectivity of 29.8%. Additionally, the concept of charge asymmetric active sites in catalysts has been explored for CO_2 reduction to C_{2+} products.[93,94] These asymmetric active-metal sites generate

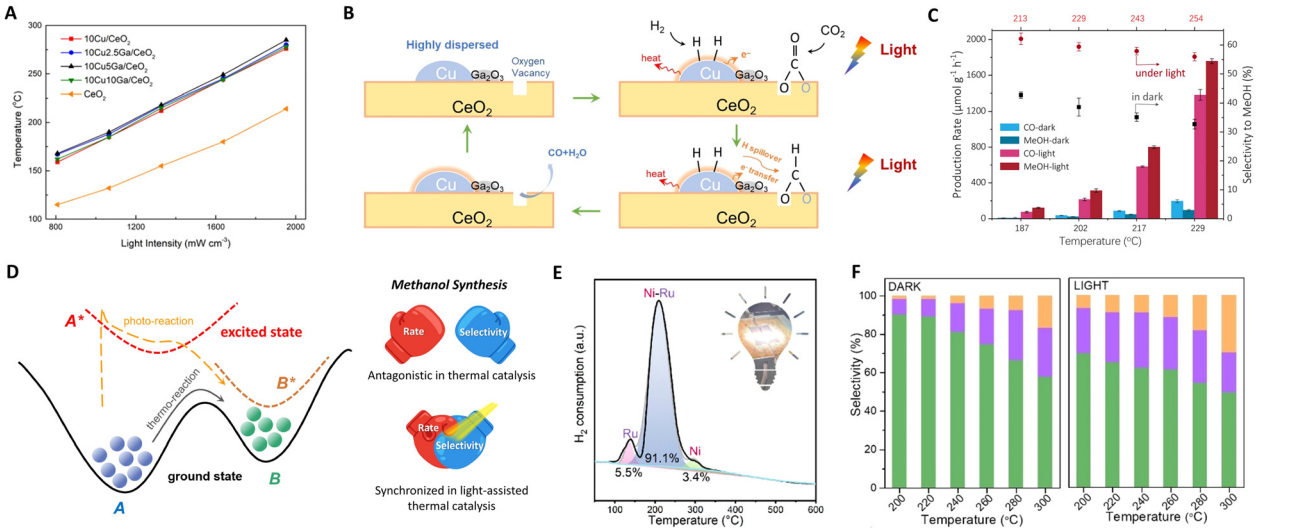

Fig. 4 (A) Solar-driven CO production over CuGaCe catalysts under different light intensities. (B) Proposed reaction mechanism for photothermal RWGS over CuGa/CeO_2. These figures have been reproduced from ref. 63 with permission from Elsevier, copyright 2021. (C) Catalytic performance on $ZnFe_2O_4$. (D) Sketch of a thermodynamic and photodynamic chemical reaction pathway. These figures have been reproduced from ref. 76 with permission from Elsevier, copyright 2023. (E) The deconvolution results of the H_2-TPR profile of the fresh Ni–Ru/HZSM-5. This figure has been reproduced from ref. 62 with permission from American Chemical Society, copyright 2023. (F) The product gas selectivity of $CoFe_2O_4$ under light and dark conditions. This figure has been reproduced from ref. 92 with permission from John Wiley & Sons, copyright 2023.

diverse charge distributions on adjacent adsorbed C_1 intermediates, reducing electrostatic repulsion and promoting C–C coupling reactions.[95,96] It is posited that the asymmetry of these catalytic active sites, along with key intermediates, not only catalyzes the C–C coupling reaction but also inhibits the hydrogenation of C_1 intermediates into C_1 products, through a synergistic mechanism at adjacent sites.[97]

3.2 Dry reforming of methane

The dry reforming of methane (DRM, eqn (1)) reaction represents a sustainable approach for mitigating CO_2 emissions, thereby addressing concurrent climate and energy crises.[98] This process transforms greenhouse gases (CO_2 and CH_4) into syngas (CO and H_2), which can subsequently be utilized in the Fischer–Tropsch process for high-value hydrocarbon production.[99,100] However, traditional DRM reactions necessitate the cleavage of the C=O bond in CO_2 (805 kJ mol^{-1}) and the C–H bond in CH_4 (434 kJ mol^{-1}), requiring thermal energy inputs and thus leading to substantial energy consumption.[101–103]

$$CO_2 + CH_4 \rightarrow 2H_2 + 2CO\left(\Delta H^{\circ}_{298K} = 247.31 \text{ kJ mol}^{-1}\right) \quad (1)$$

In response to these challenges, photothermal catalysis has been increasingly applied in this domain, offering a cleaner and milder alternative to conventional high-temperature processes.[104–106] The integration of photothermal catalysis in DRM reactions presents a significant advancement for converting CO_2 and CH_4 into valuable chemical feedstocks. This approach enhances the overall energy efficiency of the process and contributes to the reduction of greenhouse gas emissions, aligning with global environmental and energy sustainability goals.

Photon → Phonon. The application of photothermal pathways in driving the methane dry reforming (DRM) reaction has garnered significant research interest. Group VIII metals such as Ni, Co, and Pt are considered ideal catalysts for photothermal catalytic DRM. Nonetheless, these catalysts face challenges, such as rapid deactivation and pronounced carbon deposition at elevated reaction temperatures, necessitating innovative solutions. Addressing this, Li's group developed a unique nickel semi-metallic catalyst hm-Ni/Al_2O_3.[107] Under a light-driven process, remarkable yields of H_2 and CO have been reported, which could reach up to 8573.0 and 9614.3 mmol g_{Ni}^{-1} min^{-1}, respectively. In addition, compared to the 10 h deactivation in the thermal catalysis reaction, this photothermal effect (Photon → Phonon) could significantly inhibit coke deposition. The photothermal catalytic performance almost remains stable after 70 h reaction, underscoring the pivotal role of photon energy absorption in this reaction. In a recent advancement, Xu's group proposed a highly efficient photothermal catalyst Rh/$LaNiO_3$ for solar-driven DRM.[108] This catalyst enhances light-to-chemical energy efficiency (10.72%) and reduces reaction temperature, as demonstrated in Fig. 5(A) and (B). In this system, light-triggered metal-to-metal charge transfer and increased oxygen mobility significantly lower the activation energy, leading to a high conversion efficiency. Consequently, the production rates of H_2 and CO reach 452.3 and 527.6 mmol h^{-1} g_{Rh}^{-1}, respectively, under 1.5 W cm^{-2} irradiation without external heating.

Additionally, Miyauchi *et al.* reported a Rh/$SrTiO_3$ catalyst, which effectively promotes methane reforming under UV light irradiation at low temperatures.[109] The introduction of rhodium ions into the $SrTiO_3$ crystal forms impurity levels above the valence band, enhancing visible light absorbability. This catalyst efficiently utilizes photon energy for methane

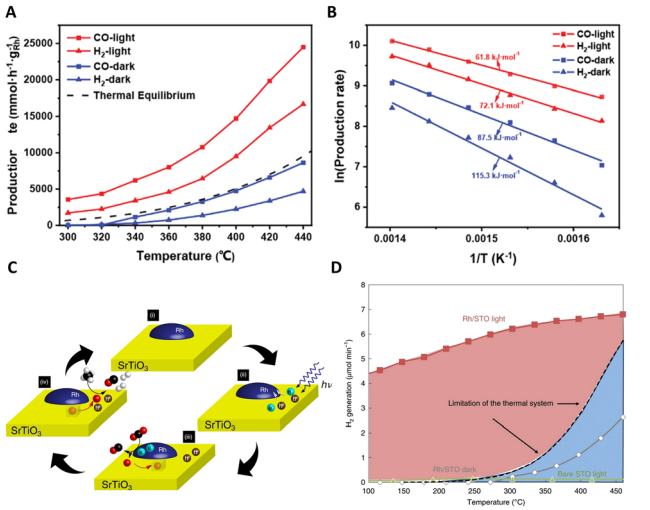

Fig. 5 (A) and (B) Production rates and apparent activation energy of H_2 and CO under irradiation or heating over Rh/$LaNiO_3$. These figures have been reproduced from ref. 108 with permission from John Wiley & Sons, copyright 2023. (C) Tentative mechanistic aspects of the photocatalytic DRM by Rh/STO. (D) The temperature dependence of DRM activity under dark and light irradiation conditions. These figures have been reproduced from ref. 109 with permission from Springer Nature, copyright 2020.

conversion with a high quantum efficiency of 5.9%. Under UV light, the excited electrons in the conduction band of STO are transferred to rhodium particles, acting as an electron acceptor in the DRM reaction and achieving efficient charge separation, as illustrated in Fig. 5(C) and (D). Electrons in Rh reduce CO_2 to CO, while photogenerated holes in the valence band of $SrTiO_3$ migrate to the interface of rhodium nanoparticles, reacting with CH_4 and O^{2-} to produce H_2. This innovative principle has potential for application in a variety of uphill reactions, where photon energy can be harnessed to overcome the limitations imposed by traditional thermodynamics and high thermal energy requirements. This approach enables the extraction of valuable products from diverse carbon resources, effectively pushing the boundaries of chemical conversion processes.

Moreover, the dual-reaction-sites catalyst Cu-CNN/Pd-BDCNN has been reported by Yin's group.[110] The strategic incorporation of copper and palladium in this catalyst serves a dual purpose: Cu and Pd act as electron and hole acceptors, respectively, while concurrently enhancing light absorption and charge separation within the catalyst. This innovative design significantly facilitates the reaction process. Remarkably, this catalyst has demonstrated a high production rate of approximately 800 μmol g^{-1} h^{-1} under light irradiation, without the need for external heating. This result underscores the efficacy and potential of dual-reaction-site strategies in the realm of photothermal catalysis, suggesting a promising avenue for future developments in this field.

Photon + Phonon. Addressing the challenges posed by the harsh conditions of traditional thermal catalysis, Zhang's group has developed a series of alumina-supported Ni_xFe_y nanoalloys for photothermal synergistic DRM, showcasing exceptional catalytic performance.[111] Under photothermal conditions, the syngas production rate reached up to 0.96 mol g^{-1} h^{-1}, a remarkable increase of approximately 1100 times compared to the same dark conditions. This significant enhancement is primarily attributed to the effective thermal activation of CO_2 under dark conditions, resulting in a relatively high apparent activation energy for DRM. Methane activation, identified as the rate-determining step, is significantly facilitated by hot electrons generated from the Localized Surface Plasmon Resonance (LSPR) effect of catalysts (hot electron injection into antibonding orbitals of CH_4) and photothermal heating under visible irradiation, as shown in Fig. 6(A) and (B). Consequently, the reaction temperature is substantially lowered, allowing the reaction to proceed at temperatures as low as 100 °C.

In an exemplary study, Ozin's group has significantly enhanced the photothermal dry reforming performance of Ni–CeO_2 by selectively phosphating the CeO_2 nanorod support surface.[112] This modification led to a remarkable increase in the H_2 : CO ratio of the produced gas from 0.44 to 0.95 under 48.1 kW m^{-2} white light irradiance at 350 °C, maintaining high stability over 50 h. A notable aspect of this research is the exploration of the disparity in catalytic efficiency between thermal and photo-assisted conditions. This exploration was conducted through the application of various light wavelengths, including ultraviolet (UV), blue, red, and green, as shown in Fig. 6(C). It was observed that blue light facilitated the most significant temperature increase, suggesting a predominantly photothermal effect. In contrast, UV light elicited a response more characteristic of photochemical processes, likely attributable to the absorption properties of the CeO_2–$CePO_4$ support. The effects under green and red light were linked to the excitation of nickel plasmon resonance. Further insights were provided by DRIFTS analysis, which confirmed an enhanced conversion of CO_2 under illumination. This was evidenced by a more pronounced CO_2 stretching peak at 2354 cm^{-1}. This study not only underscores the intricacy inherent in photothermal catalysis but also illuminates the vast potential of light manipulation in optimizing catalytic processes.

In their innovative research, Sun *et al.* delved into the dynamics of energetic hot carriers within photothermal catalytic systems, particularly focusing on the influence of external thermal effects.[113] Their study unveils a dual behavior of these carriers, which could be promoted at low to medium temperatures but experience suppression at higher temperatures due to external heating. This phenomenon is crucial as the production of thermal energy not only boosts the generation of energetic hot carriers but also reduces the redox potentials of reactants, thereby facilitating their involvement in reactions geared towards specific products, as depicted in Fig. 6(D). A critical finding of this work is the observation that at high reaction temperatures, which exceed the threshold of conventional thermal catalysis, active sites on the metal surface become predominantly occupied by thermal catalysis. This occupancy limits the availability of these sites for hot carriers, thereby reducing the effectiveness of photo-mediated catalysis. In contrast, at lower and medium temperatures where the active sites are not

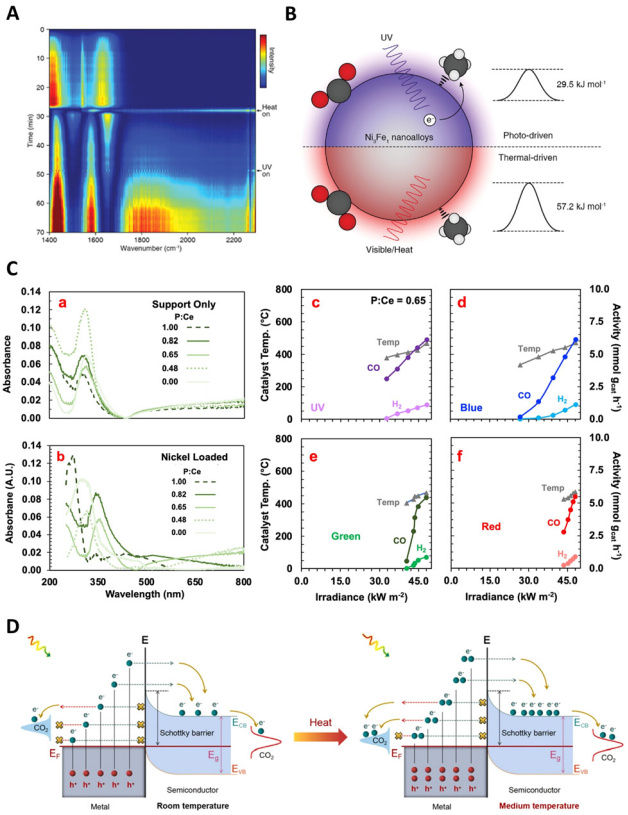

Fig. 6 (A) *In situ* DRIFT spectra for photo-driven DRM reaction on Ni_3Fe_1. (B) Schematic illustration for the photo-driven DRM reaction over the Ni_3Fe_1 nanoalloys. These figures have been reproduced from ref. 111 with permission from John Wiley & Sons, copyright 2022. (C) Wavelength dependence of the observed photothermal catalytic activity. This figure has been reproduced from ref. 112 with permission from Springer Nature, copyright 2023. (D) The schematic diagram of external thermal promotion effect on the behaviors of hot carriers. This figure has been reproduced from ref. 113 with permission from Elsevier, copyright 2022.

fully saturated, there is a noticeable improvement in the utilization of both photo-induced energetic hot carriers and thermal energy. This synergistic interaction between solar and thermal energies is most effective at medium temperatures. This aspect of the study illuminates the intricate interplay within photothermal catalysis, providing valuable insights into the efficient and practical use of solar energy in industrial applications.

Complementing these findings, Zhou's group conducted a study exploring the interplay between two primary competing reactions in the photothermal dry reforming of methane over Ni/Ga_2O_3.[114] By manipulating light irradiation, they observed a reversal in the direction of electron transfer from Ga_2O_3 to Ni, resulting in the formation of Ni^0 sites. These sites are instrumental in generating a substantial quantity of hot electrons through the electronic inter-band transition of Ni, thereby significantly enhancing both the formation and desorption of H_2. As a result of this process, the H_2/CO ratio in the production gas markedly increased from 0.55 to nearly 1. This discovery provides profound insights into the role of light irradiation in photothermal catalytic reactions and paves the way for optimizing the proportion of H_2 in C–H activation and hydrogen production processes.

3.3 NH_3 synthesis

The Haber–Bosch process, one of the seminal discoveries of the 20th century,[115] revolutionized the production of ammonia (NH_3). This innovation laid the foundation for the mass production of NH_3, which has been used to manufacture fertilizers, explosives, and other nitrogenous chemicals.[116] The core methodology of NH_3 synthesis has remained unchanged for more than a century. Approximately 95% of global NH_3 production still relies on the traditional Haber–Bosch method.[117] However, the process is inherently constrained by thermodynamic limitations. To achieve viable industrial performance, the reactors must operate under high temperatures (400 °C to 500 °C) and pressures (100 bar to 200 bar),[17] posing significant energy and environmental challenges. In sharp contrast, photocatalytic NH_3 production offers an alternative route with less energy input and ambient pressure. Thus, photothermal catalysis emerges as a promising solution, particularly in enhancing the efficiency and selectivity of NH_3 production, signifying a potential paradigm shift in this critical chemical process.

Photon → Phonon. In the realm of photocatalytic N_2 reduction, surface plasmon mechanisms play a pivotal role in facilitating N≡N bond cleavage. A notable advancement in this field was made by Xiong and colleagues, who developed a novel AuRu core-antenna nanostructure. This innovation has been shown to catalyze the dissociation of N_2 into NH_3 effectively, achieving a notable production rate of 101.4 μmol g^{-1} h^{-1} using the LSPR effect in pure water under mild conditions.[118] The design integrates a gold (Au) core to harvest light across a broad spectrum, with ruthenium (Ru) antennae serving as active sites for N_2 fixation. As illustrated in Fig. 7(A)–(C), the N_2 fixation process exhibits a near-linear dependence on light intensity, underscoring the role of plasmonic hot electrons in driving the reduction of N_2 to ammonia. This correlation is further supported by the full extinction spectra range of the AuRu nanostructures, indicating a high utilization efficiency of incident light. Specifically, the apparent quantum efficiencies (AQEs) at 350 nm and 550 nm were determined to be 0.21% and 0.17%, respectively, signifying the pivotal role of photon energy in the N_2 fixation process facilitated by the plasmonic $AuRu_x$ catalysts. Expanding on this concept, Wang's group explored the use of metal–organic framework (MOF) membranes as nanoreactors to disperse and confine gold nanoparticles (AuNPs), achieving direct plasmonic photocatalytic nitrogen fixation under ambient conditions.[119] The AuNPs generate hot electrons under visible irradiation, which are then directly injected into surface-adsorbed N_2 molecules. These molecules are activated by a strong, localized surface plasmon resonance field, which facilitates electron transfer, energy transfer, and localized-electric-field polarization effects. This results in a higher apparent quantum efficiency and lower apparent activation energy under stronger irradiation.

Furthermore, the utilization of hybrid materials in this domain has also been investigated. For instance, Wang and

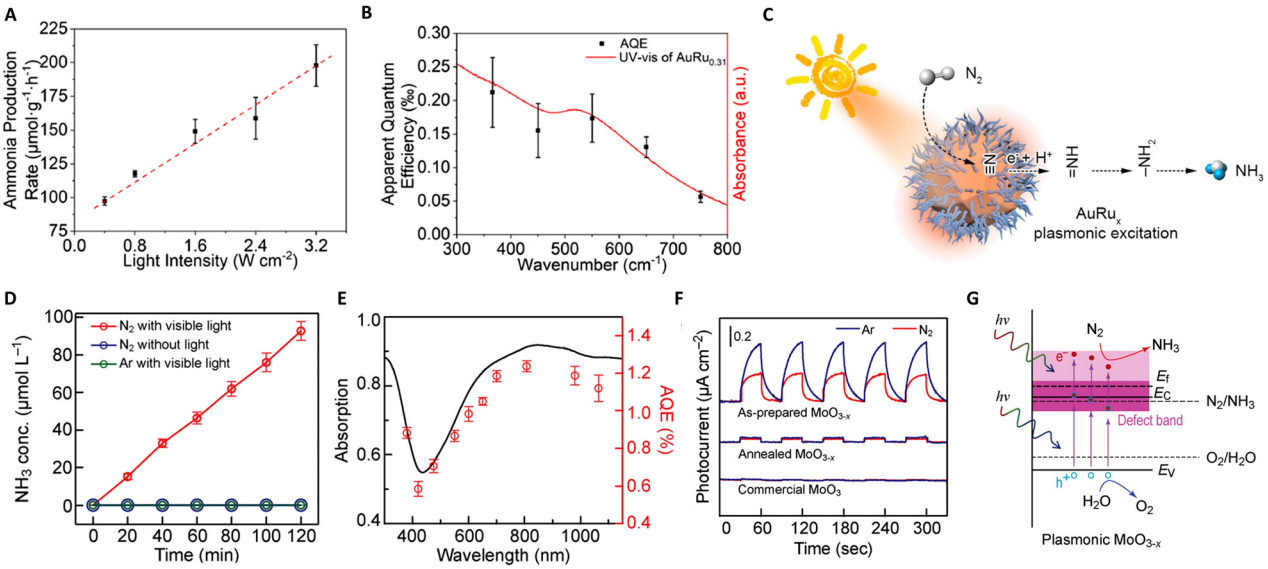

Fig. 7 (A) and (B) Photocatalytic ammonia production rates and calculated AQEs by $AuRu_{0.31}$. (C) The schematic diagram for the photo driven NH_3 synthesis over the $AuRu_{0.31}$ nanostructure. These figures have been reproduced from ref. 118 with permission from American Chemical Society, copyright 2019. (D) Photothermal catalytic NH_3 production of MoO_{3-x} under different conditions. (E) Action spectrum of the MoO_{3-x} spheres for N_2 photo-fixation. (F) Photocurrent responses of serial MoO_{3-x} spheres under an Ar and N_2 atmosphere, respectively. (G) Schematics illustrating the band structures of the plasmonic MoO_{3-x} photocatalyst. These figures have been reproduced from ref. 121 with permission from John Wiley & Sons, copyright 2021.

Zhang *et al.* developed a low-cost, plasmon-assisted Cu-based porous catalyst, $Cu_{96}Fe_4$, which achieved an NH_3 production rate of 342 μmol g_{cat}^{-1} h^{-1} without the need for sacrificial agents.[120] The Cu framework generates hot electrons through surface plasmon resonance, while the Fe atoms on the surface act as active sites for the efficient adsorption and activation of N_2. The efficient polarization of N_2 over the Fe atoms significantly decreases the reaction barrier, contributing directly to the N_2 fixation process. Nevertheless, the efficiency of these systems is often limited by the inability of hot electrons to cross the Schottky barrier, leading to their recombination with holes within the metal nanocrystal. Addressing this challenge, Wang's group introduced a Schottky-barrier-free plasmonic semiconductor, MoO_{3-x}, which demonstrates efficient N_2 fixation.[121] N_2 molecules are chemisorbed and activated at the oxygen vacancy (OV) sites in MoO_{3-x}. The abundance of electrons induced by the OVs in the conduction band creates a strong plasmon resonance on the surface of MoO_{3-x}, visible in Fig. 7(D)–(G). This unique semiconductor permits the free transport of plasmonic hot charge carriers and minimizes electron–hole recombination through defect states introduced by the OVs. As a result, this system exhibits a superior N_2 fixation ability, an apparent quantum efficiency of 1.24%, and a notable solar-to-ammonia conversion efficiency of 0.057%. This breakthrough in Schottky-barrier-free construction paves a new path for the rational design of efficient photo-thermal catalysts.

Photon + Phonon. In the quest to achieve ammonia synthesis at lower temperatures and ambient pressure, integrating photo- and thermo-catalysis has emerged as a promising strategy. A notable advancement in this field is the development of efficient and stable Ni/TiO_2 photothermal catalysts by Wang's group, facilitating ammonia production under these milder conditions.[122] In this system, photon-induced adsorption and activation of N_2 molecules occur at the TiO_2 oxygen vacancies. Simultaneously, H_2 molecules are activated by phonons generated from the thermal catalysis of Ni atoms, leading to the hydrogenation of activated nitrogen species. This synergistic effect of photo- and thermo-catalysis triggers ammonia generation at lower temperatures and ambient pressure, achieving satisfactory conversion rates.

Furthering this approach, Liu *et al.* reported a Ru-based catalyst (Ru–Cs/MgO), demonstrating efficient ammonia production with high reaction rates and yields.[123] As depicted in Fig. 8(A) and (C), the creation and control of thermal gradients *via* photothermal heating of the catalyst surfaces play a crucial role in this system. The non-isothermal gradient between the catalyst surface and its bottom promotes higher temperatures at the surface, facilitating N_2 scission, while cooler temperatures at the bottom preserve NH_3 yield. A negative gradient aligns thermophoretic forces with the reactant flow, effectively removing NH_3 from the hottest region and preventing its decomposition. Conversely, a positive gradient under the same absolute value yields lower reaction rates and product yields. These findings highlight the potential of light-induced thermal gradients as thermodynamic pumps, enhancing the catalytic activity in photo-thermal systems. Additionally, García and colleagues developed Cs-promoted ruthenium nanoparticles supported on strontium titanate (CsyRux@ST) for photothermal catalysis of NH_3 synthesis.[124] Operating under 350 °C and ambient pressure, this system achieves an impressive NH_3 production rate, surpassing dark conditions by 68%. This enhanced performance is attributed to the combined effects of photo-induced hot carrier and local thermal mechanisms at the irradiated Ru nanoparticles, facilitating N_2 activation and hydrogenation.

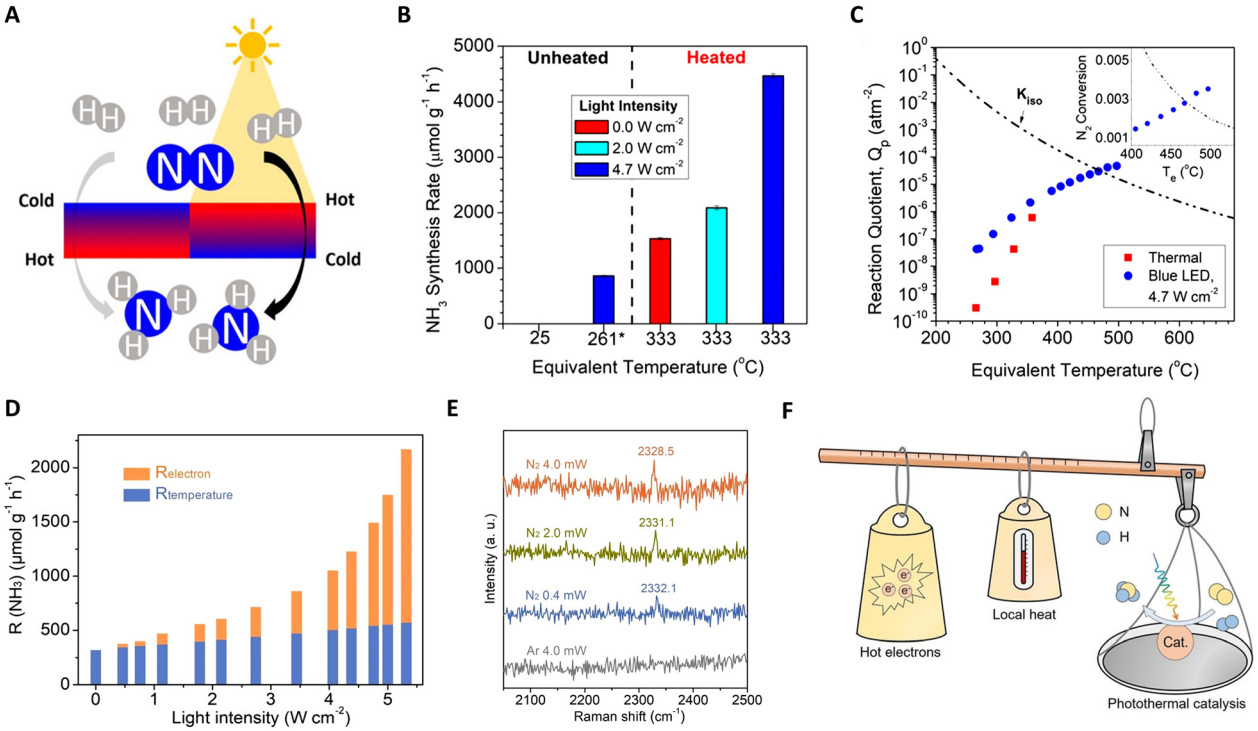

Fig. 8 (A) A schematic diagram for photo-driven NH_3 synthesis over Ru–Cs/MgO. (B) NH_3 synthesis rates under dark and additionally illuminated conditions. (C) Dependence of NH_3 synthesis and thermal gradients on illumination. These figures have been reproduced from ref. 123 with permission from American Chemical Society, copyright 2019. (D) Photothermal catalytic ammonia production rate contribution from photo-induced hot electrons ($R_{electron}$) and actual reaction temperature ($R_{temperature}$) as a function of full light intensity at $T_{apparent}$ = 350 °C. (E) *In situ* Raman spectra over the Ru/C catalyst. (F) A schematic diagram for the photo-driven NH_3 synthesis over Ru–Cs/MgO. These figures have been reproduced from ref. 125 with permission from John Wiley & Sons, copyright 2023.

While photothermal catalysis is a promising green technology, differentiating the impacts of hot electrons and local heating remains a challenge. Zhang and collaborators tackled this issue in ammonia synthesis using a Ru-loaded carbon catalyst as a model.[125] They quantified the contributions of photo-induced hot electrons and local heating effects separately using Le Chatelier's principle (non-thermal contribution ($R_{electron}$) = total photo-thermal rate (R_{PTC}) − pure thermal effects ($R_{temperature}$)), as shown in Fig. 8(D)–(F). Intriguingly, with increasing light intensity, $R_{electron}$ transitions from a linear to a super-linear relationship, confirming non-thermal effects in the system. Under specific conditions (5.0 W cm^{-2} light intensity and 350 °C), hot-electron contributions accounted for 73.6% of the total NH_3 production rate. Complementary analyses, including DRIFTS, *in situ* Raman, and kinetic experiments, further revealed that light facilitates NH_3 synthesis at lower temperatures by injecting photo-induced hot-electrons into the unoccupied anti-bonding orbitals of adsorbed N_2, aiding in N≡N bond cleavage.

3.4 Plastic upcycling

The escalating global crisis of plastic waste accumulation, posing substantial economic and health threats,[126] has prompted a keen interest in the catalytic upcycling of plastics.[127] Photothermal catalysis, an emergent technology, harnesses electromagnetic and thermal energies.[71,128] This method stands out as a sustainable alternative to energy-intensive thermocatalysis by utilizing renewable solar energy. Consequently, photothermal catalysis achieves superior catalytic performance under mild conditions, enhancing its industrial applicability. Moreover, the confluence of light and heat within this technique could potentially alter reaction pathways, steering the transformation of waste plastics into higher-value chemicals.

Photon → Phonon. The transformation of electromagnetic energy to thermal energy *via* the photothermal effect can elevate surrounding temperatures.[129] In the context of metal nanoparticles, the hot charge carriers produced by photoinduced localized surface plasmon resonance (LSPR) can decay, releasing energy to heat surface adsorbates (photon → phonon), thereby accelerating catalytic reactions.[130] In a pioneering study in 2019, Firestone's group introduced photothermal-driven thermal-oxidative degradation of plastic waste.[131] In their system, dilute silver nanoparticles (AgNPs) were embedded in low-density polyethylene. Under intense and resonant light irradiation, the heat generated from the photon → phonon process expedited the action of the thermal pro-oxidant cobalt stearate on LDPE, matching the rate observed in a 60 °C oven. The photothermal effect of AgNPs was evidenced by a stronger carboxylic acid FTIR signal and ketone UV-vis signal in PE–AgNP–Co samples under blue light, as shown in Fig. 9(A). Huang's group further explored the LSPR

effect of AgNPs in driving thermo-oxidative depolymerization of polyethylcyanoacrylate (PECA) and starch composites.[132] The depolymerization predominantly occurred around the AgNPs, creating mesoscopic defect sites within the PECA–starch composite film and reducing its tensile strength. These findings highlight the presence of a heterogeneous temperature field in photothermal heating, crucial for developing new plastic waste management methods.

Recent focus has shifted towards photothermal upcycling of plastics, treating waste as a source of recoverable chemicals rather than material for CO_2 mineralization. Chen *et al.* developed a multi-walled carbon nanotube modified by polydopamine (CNT-PDA) for PET depolymerization.[133] Under solar irradiation, CNT-PDA serves as a light absorber, converting solar energy into thermal energy to drive PET depolymerization, as depicted in Fig. 9(B) and (C). The absorbers first efficiently convert sunlight to thermal energy, enabling PET depolymerization into BHET *via* a nucleophilic addition–elimination mechanism in the presence of an organic catalyst (cholinium phosphate). Solar thermal catalysis exhibited thrice the recycling efficiency of thermal catalysis due to localized heating effects. In the same vein, they introduced cobalt single-site catalysts (Co SSCs) on CNT-PDA for photothermally catalyzing polyester upcycling.[134] The Co-O_5 single-site coordinates with polyester carbonyl groups, enhancing nucleophilic addition–elimination processes, as shown in Fig. 9(D) and (E). The space-time yield of Co SSCs was significantly higher than general catalysts, and PET conversion and bis(2-hydroxyethyl) terephthalate yield in photothermal catalysis surpassed those in thermal catalysis (5.4 and 6.6 times). Technical economic analysis revealed that recycling 10^5 tons of waste PET through photothermal catalysis consumes 146.4 GW h of electrical energy and reduces CO_2 emissions by 7.44×10^4 tons. Thus, an efficient photothermal catalytic system for plastic recycling has immense potential for waste plastic valorization.

Photon + Phonon. Incident photons could be harnessed through various pathways to maximize energy conversion efficiency in photothermal catalysis. High-energy photons with short wavelengths excite photocatalysts, driving photochemical redox reactions.[135] In contrast, low-energy photons with longer wavelengths generate heat from phonon interactions to accelerate photocatalytic reactions or initiate thermal catalytic processes. An exemplary study by Ma's group on the heterogeneous catalytic oxidation of polystyrene using g-C_3N_4 highlights this phenomenon.[136] Under 150 °C heating without light, g-C_3N_4 exhibited minimal catalytic activity (<5% conversion over 40 h). However, under simultaneous light irradiation and heating, the conversion of the polystyrene substrate exceeded 50% in just 10 h. This significant rate increase is attributed to the formation of $^{\bullet}O^{2-}$ radicals, exclusive to light irradiation in the presence of g-C_3N_4, crucial for C–C skeleton fracture in polystyrene, as illustrated in Fig. 10(A)–(C). The phonon effect (high temperature) primarily enhances PS solubility and promotes mass transfer and diffusion during the reaction. In addition, Yin *et al.* developed a photochromic-photothermal catalytic system based on polyol-ligated TiO_2 nanocrystals.[137] Upon UV or sunlight exposure, photogenerated holes in TiO_2 captured DEGs on the surface, leading to oxygen vacancies and

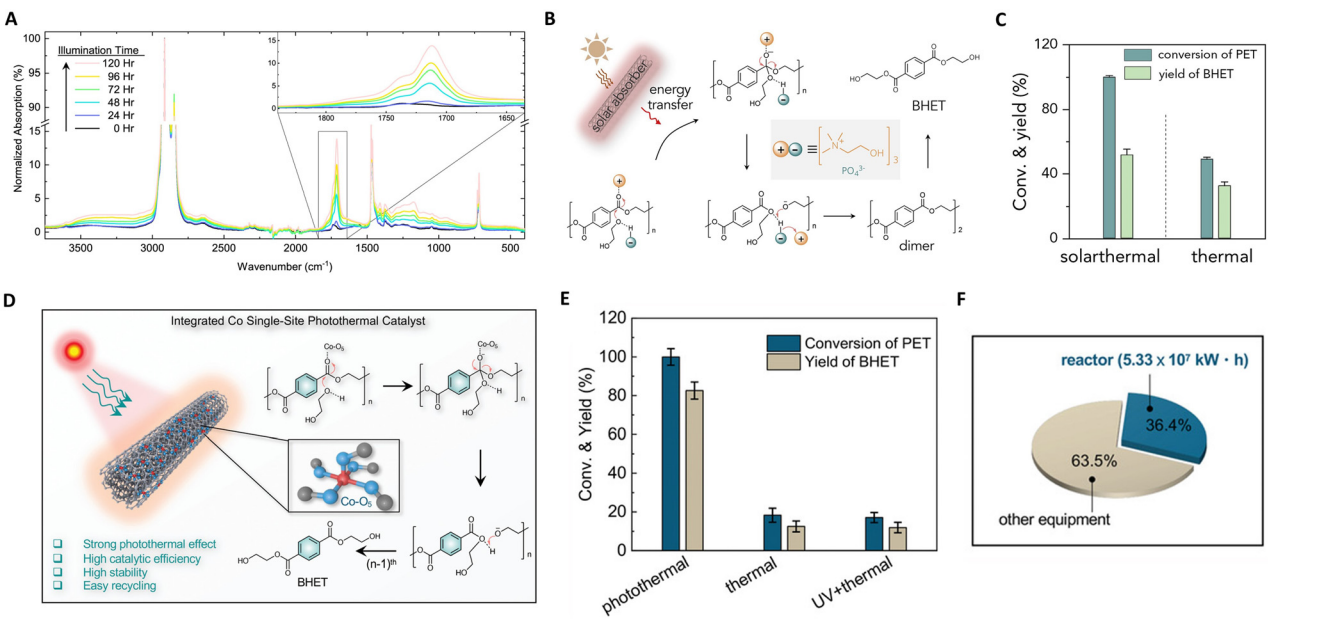

Fig. 9 (A) Infrared spectra of PE-AgNP-Co as a function of illumination time. This figure has been reproduced from ref. 131 with permission from IOP Publishing, copyright 2019. (B) The proposed mechanism of the photothermal upcycling of PET. (C) The proposed mechanism of the photothermal upcycling of PET. These figures have been reproduced from ref. 133 with permission from Elsevier, copyright 2022. (D) Integrated functionalities of Co SSCs and the photothermal catalytic mechanism of PET glycolysis over Co SSCs. (E) Conversions and yields of upcycling of PET over Co SSCs under different reaction conditions. (F) Energy consumption evaluation of Co SSCs. These figures have been reproduced from ref. 134 with permission from John Wiley & Sons, copyright 2022.

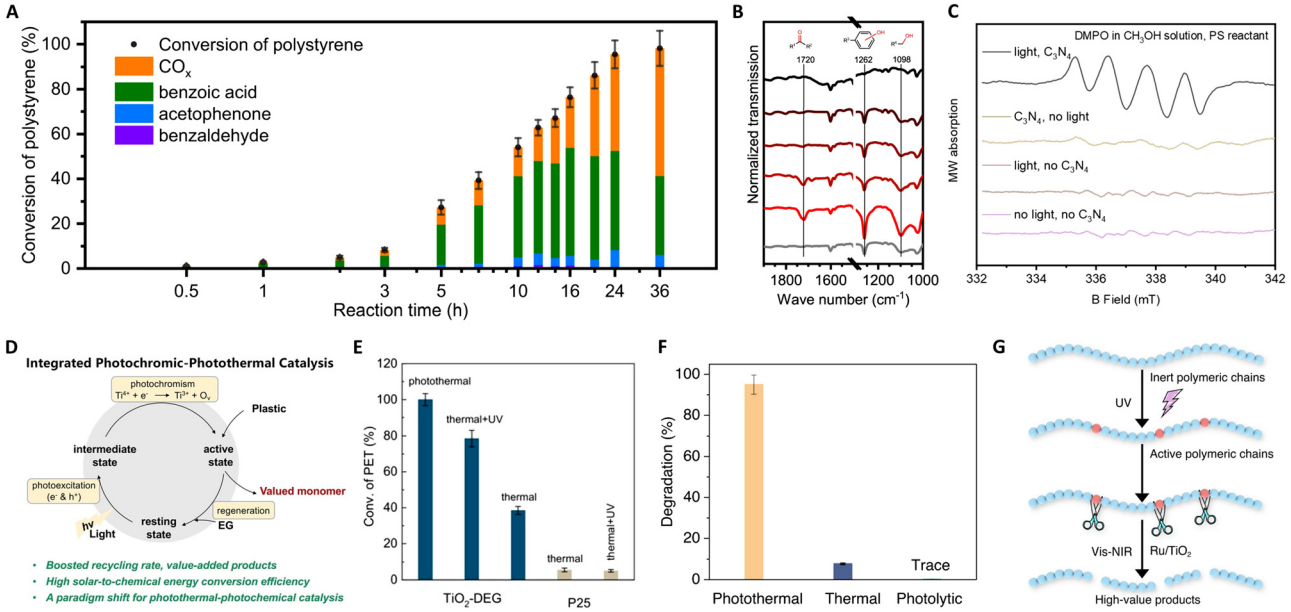

Fig. 10 (A) Time-evolution of different products for polystyrene photothermal catalytic reaction at 150 °C. (B) The infrared (IR) transmission spectra of the polystyrene reactant and the recovered polystyrene after reactions with light irradiation for 0 h, 0.5 h, 2 h, 5 h, and 10 h and without light irradiation for 10 h. (C) EPR spectra under different illumination and catalyst conditions. These figures have been reproduced from ref. 136 with permission from Springer Nature, copyright 2022. (D) Schematic illustration of the proposed photothermal reaction mechanism. (E) Catalytic performance evaluation of TiO_2-DEG *via* PET glycolysis. These figures have been reproduced from ref. 137 with permission from John Wiley & Sons, copyright 2023. (F) Degradation percentages of LDPE under photothermal (300 °C), thermal (300 °C), and photolysis under ambient temperature conditions. (G) Schematic illustration of the proposed photothermal reaction mechanism. These figures have been reproduced from ref. 139 with permission from Springer Nature, copyright 2023.

the reduction of Ti^{4+} to Ti^{3+}. The resulting black TiO_2 showed enhanced sunlight absorption and thermal energy generation *via* non-radiative decay. This system achieved performance enhancements of 6-fold and 12.2-fold under thermal and photothermal conditions, respectively, compared to commercial TiO_2, as shown in Fig. 10(D) and (E).

Furthermore, Zeng's group pioneered the use of concentrated solar energy for photothermal catalytic upcycling of polyolefin waste, devising a photothermal catalytic pyrolysis apparatus capable of reaching 500 °C.[138] Their results with a Ni–Ti–Al catalyst demonstrated significant hydrogen production (34 mol kg^{-1}) and jet fuel selectivity (80%), attributed to the interplay between photogenerated electrons in plasmonic metal Ni and the carrier transfer capability of non-plasmonic semiconductor TiO_2. This method offers an eco-friendly approach to the high-value recycling of waste plastics into hydrogen and jet fuel. In a notable advancement, Zhang's group reported on the photothermal pyrolysis of polyolefin plastics (LDPE, HDPE, UHMWPE, PP, and commercial LDPE bags) using a Ru/TiO_2 catalyst.[139] This method significantly outperforms traditional thermal catalysis, exhibiting a tenfold increase in efficiency under photothermal conditions compared to dark conditions. The key to this process is the use of UV light to activate the polymeric chains, which are then efficiently decomposed from polyolefin plastics into lower molecular-weight molecules by Ru nanoparticles, as shown in Fig. 10(F) and (G). Additionally, the application of Vis and NIR light irradiation induces localized heating, melting the polymers for optimal catalyst contact, and facilitating C–C bond scission on Ru sites. Remarkably, this approach enables the complete conversion of waste polyolefins into valuable liquid fuels, mainly gasoline (86%) and diesel-range hydrocarbons (C_5–C_{21}), within a short 3-hour timeframe. Crucially, the system demonstrates high efficiency under concentrated sunlight, representing a significant stride towards sustainable, solar-driven plastic waste recycling.

4. Conclusions and perspective

Photothermal catalysis, a process energized by both photon and phonon interactions, has recently emerged as a cutting-edge strategy for achieving sustainable and clean energy and chemical production. In this innovative approach, thermal energy, conveyed through phonons, can be supplied externally or generated from photons, effectively reducing the reaction barrier by increasing temperature. This conversion of electromagnetic to thermal energy is efficiently facilitated *via* mechanisms such as localized surface plasmon resonance (LSPR) or non-radiative relaxation in semiconductors, distinguishing it from conventional photocatalysis and thermocatalysis. The former often encounters limitations in photon utilization efficiency, particularly within the visible light spectrum, whereas the latter demands severe reaction conditions.

However, photothermal catalysis harnesses the synergistic effects of photons and phonons to markedly improve catalytic reactions. Utilizing renewable solar irradiation, this method enables the transformation or coupling of photons with

phonons, showcasing several advantages: (i) milder reaction conditions compared to thermocatalysis, (ii) enhanced reaction rates and selectivity, and (iii) increased stability and minimized sintering of the active phase. These collective benefits highlight the significant potential of photothermal catalysis in producing solar fuels.

However, some existing problems and challenges should also be attended to and solved. (i) In-depth understanding of the mechanism of photothermal catalysis is key to controlling the reaction and selectivity of the desired products. However, the difficulty in the detection of some transitional species and a significant lack of understanding of the nature of reaction intermediates are the barriers to the next step. (ii) Economic photothermal catalysts with a strong ability to absorb lower-energy regions in the electromagnetic spectrum are highly desired. In general, most photocatalyst materials show light absorption around 300–500 nm, with weak visible light absorption above 600 nm. Unfortunately, the energy of solar light is mainly in the latter region. Improving the utilization of a wider solar spectrum is worth consideration. Due to the aim of pilot plants and industrialization, the cost and mild reaction conditions of catalysts are also critical. (iii) The xenon lamps' light intensity is around 20–50 times higher than that of natural light. Direct utilization of solar energy is challenging, highlighting the need for designing ideal reactors that are capable of harnessing solar energy effectively.

This review delves into the mechanisms and applications of photothermal catalysis, examining both photon and phonon contributions. This analysis aims to not only clarify the field but also to inspire future research. (i) For the mechanism research, integrating advanced *in situ* characterization techniques and computational calculations promises to enrich the understanding and enable direct observations from both photon and phonon perspectives. For instance, femtosecond infrared laser pulses were used to observe the reaction dynamics of photothermal catalysis *via* the desorption and oxidation of CO on Ru(0001), thus revealing the slower CO desorption coupling to phonons ($\sim$20 ps) and the faster oxidation of CO driven by the hot electrons ($\sim$3 ps).[140]

(ii) In the realm of catalyst design, tuning the surface of catalysts to black has been identified as a promising strategy for directly converting UV-VIS-IR light into thermal energy.[34,59] Concurrently, the expanding comprehension of photochemical and thermal interactions within nanostructured catalysts will advocate for the continuous exploration and development of materials characterized by broadband absorption and high responsiveness. Moreover, high temperatures can potentially skew the equilibrium of the reaction system in gas-phase heterogeneous exothermic reactions.[24] Therefore, the strategic implementation of thermal management within catalyst systems emerges as a critical factor in maintaining the delicate equilibrium necessary for optimal catalytic function. For instance, the advent of 3D-printed metallic and ceramic structures, serving as conduits for fluid, signifies a breakthrough in enhancing thermal energy and mass transfer within catalytic flow systems.[141] This inspiring idea of heat management for the fabrication of photothermal catalysts may offer a novel paradigm in catalyst design.

(iii) Continuous flow operation is better suited for large-scale photothermal processes. Elongated and reflective parabolic surfaces were used to focus light onto a transparent tube through which the reactant flows. Nevertheless, the inherent variability of solar illumination due to natural day/night cycles and changes in solar angle presents significant challenges for the industrial application of photothermal catalysis. Hence, the development of reactors for capturing, focusing, and storing solar energy is of paramount importance. For example, IMDEA Energy in Spain realized the solar tower fuel plant,[142] which seamlessly integrates a solar tower concentrating facility, a solar reactor, and a gas-to-liquid unit. Within this framework, the 50-kW solar reactor demonstrated its capability by performing 62 consecutive redox cycles over 9 days, culminating in the production of approximately 5191 L of syngas. Furthermore, the thermal radiation of high-temperature catalytic reactions seems to be beneficial in improving the overall catalytic performance. Our research group recently proposed thermal radiative catalysis that utilizes high temperature and its corresponding thermal radiation to facilitate ethane dehydrogenation reaction, whereas the catalytic performance will not be influenced by external light sources.[143] These notable accomplishments underscore the vast potential of electromagnetic energy in powering large-scale chemical manufacturing processes and serve as a beacon for future research directions.

Photothermal catalysis represents a broad definition of reactions where both thermal energy and electromagnetic energy (photons and phonons) are involved, necessitating an unambiguous classification. Such comprehensive insights into the interplay between photons and phonons are expected to lead to novel catalytic paradigms, inspire innovative catalyst preparation methods, and design targeted reactors. These kinds of high energy efficiency and precise process control approaches are poised to improve the overall catalytic performance further. Ultimately, we foresee that photothermal systems will achieve record performances, potentially opening a new pathway for sustainable chemical and fuel production.

Author contributions

Chang Xu: conceptualization, validation, formal analysis, investigation, data curation, writing – original draft, and writing – review and editing. Qijun Tang: conceptualization, validation, formal analysis, investigation, data curation, writing – original draft, and writing – review and editing. Wenguang Tu*: writing – original draft, writing – review and editing, resources, funding acquisition, supervision, and project administration. Lu Wang*: writing – original draft, writing – review and editing, resources, funding acquisition, supervision, and project administration.

Conflicts of interest

There are no conflicts to declare.

Acknowledgements

All authors appreciate the support from the National Key R&D Program of China (grants no. 2021YFF0502000), the National Natural Science Foundation of China (grants no. 52102311 and 52202306), Shenzhen Natural Science Foundation 2022, Provincial Talent Plan (grants no. 2023TB0012 and 2023TB0006), the University Development Fund (grants no. UDF01001721), the Program from Guangdong Introducing Innovative and Entrepreneurial Teams (2019ZT08L101 and RCTDPT-2020-001), the Shenzhen Key Laboratory of Eco-materials and Renewable Energy (ZDSYS202009-22160400001), and the Shenzhen Natural Science Foundation (GXWD20201231105722002-20200824163747001). Dedicated to Professor Geoffrey A. Ozin's 80th birthday.

Notes and references

1 D. Gielen, F. Boshell, D. Saygin, M. D. Bazilian, N. Wagner and R. Gorini, *Energy Strategy Rev.*, 2019, **24**, 38–50.
2 S. Paraschiv and L. S. Paraschiv, *Energy Rep.*, 2020, **6**, 237–242.
3 K. K. Jaiswal, C. R. Chowdhury, D. Yadav, R. Verma, S. Dutta, K. S. Jaiswal, B. Sangmesh and K. S. K. Karuppasamy, *Energy Nexus*, 2022, **7**, 100118.
4 M. S. Nazir, A. J. Mahdi, M. Bilal, H. M. Sohail, N. Ali and H. M. N. Iqbal, *Sci. Total Environ.*, 2019, **683**, 436–444.
5 J. W. Lund and A. N. Toth, *Geothermics*, 2021, **90**, 101915.
6 A. F. d O. Falcão, *Renewable Sustainable Energy Rev.*, 2010, **14**, 899–918.
7 N. Kannan and D. Vakeesan, *Renewable Sustainable Energy Rev.*, 2016, **62**, 1092–1105.
8 Y. Izumi, *Coord. Chem. Rev.*, 2013, **257**, 171–186.
9 O. A. Al-Shahri, F. B. Ismail, M. A. Hannan, M. S. H. Lipu, A. Q. Al-Shetwi, R. A. Begum, N. F. O. Al-Muhsen and E. Soujeri, *J. Cleaner Prod.*, 2021, **284**, 125465.
10 S. Faisal Ahmed, M. Khalid, M. Vaka, R. Walvekar, A. Numan, A. Khaliq Rasheed and N. Mujawar Mubarak, *Therm. Sci. Eng. Prog.*, 2021, **25**, 100981.
11 C. Xu, P. Ravi Anusuyadevi, C. Aymonier, R. Luque and S. Marre, *Chem. Soc. Rev.*, 2019, **48**, 3868–3902.
12 S. Sarina, E. R. Waclawik and H. Zhu, *Green Chem.*, 2013, **15**, 1814–1833.
13 K. K. Ghuman, L. B. Hoch, P. Szymanski, J. Y. Y. Loh, N. P. Kherani, M. A. El-Sayed, G. A. Ozin and C. V. Singh, *J. Am. Chem. Soc.*, 2016, **138**, 1206–1214.
14 C. Song, Z. Wang, Z. Yin, D. Xiao and D. Ma, *Chem. Catal.*, 2022, **2**, 52–83.
15 P. C. Angelomé, H. Heidari Mezerji, B. Goris, I. Pastoriza-Santos, J. Pérez-Juste, S. Bals and L. M. Liz-Marzán, *Chem. Mater.*, 2012, **24**, 1393–1399.
16 X. Bian, Y. Zhao, G. I. N. Waterhouse, Y. Miao, C. Zhou, L.-Z. Wu and T. Zhang, *Angew. Chem., Int. Ed.*, 2023, **62**, e202304452.
17 D. Mateo, J. L. Cerrillo, S. Durini and J. Gascon, *Chem. Soc. Rev.*, 2021, **50**, 2173–2210.
18 S. Fang and Y. H. Hu, *Chem. Soc. Rev.*, 2022, **51**, 3609–3647.
19 S. Du, X. Bian, Y. Zhao, R. Shi and T. Zhang, *Chem. Res. Chin. Univ.*, 2022, **38**, 723–734.
20 J. Zhang, H. Chen, X. Duan, H. Sun and S. Wang, *Mater. Today*, 2023, **68**, 234–253.
21 L. Wang, Y. Dong, T. Yan, Z. Hu, F. M. Ali, D. M. Meira, P. N. Duchesne, J. Y. Y. Loh, C. Qiu, E. E. Storey, Y. Xu, W. Sun, M. Ghoussoub, N. P. Kherani, A. S. Helmy and G. A. Ozin, *Nat. Commun.*, 2020, **11**, 2432.
22 D. Takami, J. Tsubakimoto, W. Sarwana, A. Yamamoto and H. Yoshida, *ACS Appl. Energy Mater.*, 2023, **6**, 7627–7635.
23 C. Mao, H. Li, H. Gu, J. Wang, Y. Zou, G. Qi, J. Xu, F. Deng, W. Shen, J. Li, S. Liu, J. Zhao and L. Zhang, *Chem*, 2019, **5**, 2702–2717.
24 M. Ghoussoub, M. Xia, P. N. Duchesne, D. Segal and G. Ozin, *Energy Environ. Sci.*, 2019, **12**, 1122–1142.
25 A. Bansal, J. S. Sekhon and S. S. Verma, *Plasmonics*, 2014, **9**, 143–150.
26 M. P. Singh and G. F. Strouse, *J. Am. Chem. Soc.*, 2010, **132**, 9383–9391.
27 N. Jiang, X. Zhuo and J. Wang, *Chem. Rev.*, 2018, **118**, 3054–3099.
28 D. Mateo, J. L. Cerrillo, S. Durini and J. Gascon, *Chem. Soc. Rev.*, 2021, **50**, 2173–2210.
29 U. Aslam, V. G. Rao, S. Chavez and S. Linic, *Nat. Catal.*, 2018, **1**, 656–665.
30 X. Li, D. Xiao and Z. Zhang, *New J. Phys.*, 2013, **15**, 023011.
31 S. Luo, X. Ren, H. Lin, H. Song and J. Ye, *Chem. Sci.*, 2021, **12**, 5701–5719.
32 M. L. Brongersma, N. J. Halas and P. Nordlander, *Nat. Nanotechnol.*, 2015, **10**, 25–34.
33 S. Yu, A. J. Wilson, G. Kumari, X. Zhang and P. K. Jain, *ACS Energy Lett.*, 2017, **2**, 2058–2070.
34 Z. Zhang, C. Mao, D. M. Meira, P. N. Duchesne, A. A. Tountas, Z. Li, C. Qiu, S. Tang, R. Song, X. Ding, J. Sun, J. Yu, J. Y. Howe, W. Tu, L. Wang and G. A. Ozin, *Nat. Commun.*, 2022, **13**, 1512.
35 A. Gellé, T. Jin, L. de la Garza, G. D. Price, L. V. Besteiro and A. Moores, *Chem. Rev.*, 2020, **120**, 986–1041.
36 X. Yang and D. Wang, *ACS Appl. Energy Mater.*, 2018, **1**, 6657–6693.
37 Y. Zhao, W. Gao, S. Li, G. R. Williams, A. H. Mahadi and D. Ma, *Joule*, 2019, **3**, 920–937.
38 V. Jain, R. K. Kashyap and P. P. Pillai, *Adv. Opt. Mater.*, 2022, **10**, 2200463.
39 J. Zhou, H. Liu and H. Wang, *Chin. Chem. Lett.*, 2023, **34**, 107420.
40 F. Pan, X. Xiang, Z. Du, E. Sarnello, T. Li and Y. Li, *Appl. Catal., B*, 2020, **260**, 118189.
41 B. Xie, D. Hu, P. Kumar, V. V. Ordomsky, A. Y. Khodakov and R. Amal, *Joule*, 2024, **8**, 312–333.
42 K. K. Ghuman, T. E. Wood, L. B. Hoch, C. A. Mims, G. A. Ozin and C. V. Singh, *Phys. Chem. Chem. Phys.*, 2015, **17**, 14623–14635.
43 Z. Zhang, H. Tian, J. Sun, D. M. Meira, M. Zhang, X. Ding, D. Ji, C. Qiu, Z. Lu, L. Sun, Y. Zhang, W. Tu, Y. Zhou, X. Yang, J. Howe, L. Wang, S.-Y. Tong and Z. Zou, *Chem. Catal.*, 2023, **3**, 100644.

44 J. J. Mock, M. Barbic, D. R. Smith, D. A. Schultz and S. Schultz, *J. Chem. Phys.*, 2002, **116**, 6755–6759.
45 J. Zhang, H. Liu, Z. Wang and N. Ming, *Adv. Funct. Mater.*, 2007, **17**, 3295–3303.
46 A. Manjavacas, J. G. Liu, V. Kulkarni and P. Nordlander, *ACS Nano*, 2014, **8**, 7630–7638.
47 S. Dal Forno, L. Ranno and J. Lischner, *J. Phys. Chem. C*, 2018, **122**, 8517–8527.
48 M. Rycenga, C. M. Cobley, J. Zeng, W. Li, C. H. Moran, Q. Zhang, D. Qin and Y. Xia, *Chem. Rev.*, 2011, **111**, 3669–3712.
49 S. Link and M. A. El-Sayed, *J. Phys. Chem. B*, 1999, **103**, 4212–4217.
50 Q. Zhang, W. Li, C. Moran, J. Zeng, J. Chen, L.-P. Wen and Y. Xia, *J. Am. Chem. Soc.*, 2010, **132**, 11372–11378.
51 S. Link and M. A. El-Sayed, *Int. Rev. Phys. Chem.*, 2000, **19**, 409–453.
52 B. J. Wiley, Y. Chen, J. M. McLellan, Y. Xiong, Z.-Y. Li, D. Ginger and Y. Xia, *Nano Lett.*, 2007, **7**, 1032–1036.
53 B. J. Wiley, Y. Xiong, Z.-Y. Li, Y. Yin and Y. Xia, *Nano Lett.*, 2006, **6**, 765–768.
54 M. J. Mulvihill, X. Y. Ling, J. Henzie and P. Yang, *J. Am. Chem. Soc.*, 2010, **132**, 268–274.
55 H. Zhang and A. O. Govorov, *J. Phys. Chem. C*, 2014, **118**, 7606–7614.
56 L. V. Besteiro and A. O. Govorov, *J. Phys. Chem. C*, 2016, **120**, 19329–19339.
57 G. Baffou, R. Quidant and F. J. García de Abajo, *ACS Nano*, 2010, **4**, 709–716.
58 G. Baffou, R. Quidant and C. Girard, *Appl. Phys. Lett.*, 2009, **94**, 153109.
59 L. Wang, Y. Dong, T. Yan, Z. Hu, F. M. Ali, D. M. Meira, P. N. Duchesne, J. Y. Y. Loh, C. Qiu, E. E. Storey, Y. Xu, W. Sun, M. Ghoussoub, N. P. Kherani, A. S. Helmy and G. A. Ozin, *Nat. Commun.*, 2020, **11**, 2432.
60 K. Manthiram and A. P. Alivisatos, *J. Am. Chem. Soc.*, 2012, **134**, 3995–3998.
61 W. Wei, Z. Wei, R. Li, Z. Li, R. Shi, S. Ouyang, Y. Qi, D. L. Philips and H. Yuan, *Nat. Commun.*, 2022, **13**, 3199.
62 X. Yan, M. Cao, S. Li, P. N. Duchesne, W. Sun, C. Mao, R. Song, Z. Lu, X. Chen, W. Qian, R. Li, L. Wang and G. A. Ozin, *J. Am. Chem. Soc.*, 2023, **145**, 27358–27366.
63 B. Deng, H. Song, K. Peng, Q. Li and J. Ye, *Appl. Catal., B*, 2021, **298**, 120519.
64 Y.-Z. Chen, Z. U. Wang, H. Wang, J. Lu, S.-H. Yu and H.-L. Jiang, *J. Am. Chem. Soc.*, 2017, **139**, 2035–2044.
65 D. Kumar, C. H. Park and C. S. Kim, *ACS Sustainable Chem. Eng.*, 2018, **6**, 8604–8614.
66 M. V. Balois, N. Hayazawa, F. C. Catalan, S. Kawata, T.-A. Yano and T. Hayashi, *Anal. Bioanal. Chem.*, 2015, **407**, 8205–8213.
67 W. Sun, G. Zhong, C. Kubel, A. A. Jelle, C. Qian, L. Wang, M. Ebrahimi, L. M. Reyes, A. S. Helmy and G. A. Ozin, *Angew. Chem., Int. Ed.*, 2017, **56**, 6329–6334.
68 J. Jia, H. Wang, Z. Lu, P. G. O'Brien, M. Ghoussoub, P. Duchesne, Z. Zheng, P. Li, Q. Qiao, L. Wang, A. Gu, A. A. Jelle, Y. Dong, Q. Wang, K. K. Ghuman, T. Wood, C. Qian, Y. Shao, C. Qiu, M. Ye, Y. Zhu, Z. H. Lu, P. Zhang, A. S. Helmy, C. V. Singh, N. P. Kherani, D. D. Perovic and G. A. Ozin, *Adv. Sci.*, 2017, **4**, 1700252.
69 M. Cai, Z. Wu, Z. Li, L. Wang, W. Sun, A. A. Tountas, C. Li, S. Wang, K. Feng, A.-B. Xu, S. Tang, A. Tavasoli, M. Peng, W. Liu, A. S. Helmy, L. He, G. A. Ozin and X. Zhang, *Nat. Energy*, 2021, **6**, 807–814.
70 S. Li, P. Miao, Y. Zhang, J. Wu, B. Zhang, Y. Du, X. Han, J. Sun and P. Xu, *Adv. Mater.*, 2021, **33**, e2000086.
71 J. Sun, W. Sun, L. Wang and G. A. Ozin, *Acc. Mater. Res.*, 2022, **3**, 1260–1271.
72 L. B. Hoch, T. E. Wood, P. G. O'Brien, K. Liao, L. M. Reyes, C. A. Mims and G. A. Ozin, *Adv. Sci.*, 2014, **1**, 1400013.
73 F. Sastre, A. V. Puga, L. Liu, A. Corma and H. Garcia, *J. Am. Chem. Soc.*, 2014, **136**, 6798–6801.
74 Y. Qi, L. Song, S. Ouyang, X. Liang, S. Ning, Q. Zhang and J. Ye, *Adv. Mater.*, 2020, **32**, e1903915.
75 Y. F. Xu, P. N. Duchesne, L. Wang, A. Tavasoli, F. M. Ali, M. Xia, J. F. Liao, D. B. Kuang and G. A. Ozin, *Nat. Commun.*, 2020, **11**, 5149.
76 Y.-F. Xu, A. A. Tountas, R. Song, J. Ye, J.-H. Wei, S. Ji, L. Zhao, W. Zhou, J.-H. Chen, G. Zhao, X. Yao, M. M. Sain, D.-B. Kuang and G. A. Ozin, *Joule*, 2023, **7**, 738–752.
77 L. Wang, M. Ghoussoub, H. Wang, Y. Shao, W. Sun, A. A. Tountas, T. E. Wood, H. Li, J. Y. Y. Loh, Y. Dong, M. Xia, Y. Li, S. Wang, J. Jia, C. Qiu, C. Qian, N. P. Kherani, L. He, X. Zhang and G. A. Ozin, *Joule*, 2018, **2**, 1369–1381.
78 X. Yu, X. Ding, Y. Yao, W. Gao, C. Wang, C. Wu, C. Wu, B. Wang, L. Wang and Z. Zou, *Adv. Mater.*, 2024, e2312942, DOI: **10.1002/adma.202312942**.
79 Y. Chen, Y. Zhang, G. Fan, L. Song, G. Jia, H. Huang, S. Ouyang, J. Ye, Z. Li and Z. Zou, *Joule*, 2021, **5**, 3235–3251.
80 H. Jiang, L. Wang, H. Kaneko, R. Gu, G. Su, L. Li, J. Zhang, H. Song, F. Zhu, A. Yamaguchi, J. Xu, F. Liu, M. Miyauchi, W. Ding and M. Zhong, *Nat. Catal.*, 2023, **6**, 519–530.
81 Z. Lu, Y. Xu, Z. Zhang, J. Sun, X. Ding, W. Sun, W. Tu, Y. Zhou, Y. Yao, G. A. Ozin, L. Wang and Z. Zou, *J. Am. Chem. Soc.*, 2023, **145**, 26052–26060.
82 J. Wei, Q. Ge, R. Yao, Z. Wen, C. Fang, L. Guo, H. Xu and J. Sun, *Nat. Commun.*, 2017, **8**, 15174.
83 P. Gao, S. Li, X. Bu, S. Dang, Z. Liu, H. Wang, L. Zhong, M. Qiu, C. Yang, J. Cai, W. Wei and Y. Sun, *Nat. Chem.*, 2017, **9**, 1019–1024.
84 S. Ning, H. Ou, Y. Li, C. Lv, S. Wang, D. Wang and J. Ye, *Angew. Chem., Int. Ed.*, 2023, **62**, e202302253.
85 O. Martin, A. J. Martin, C. Mondelli, S. Mitchell, T. F. Segawa, R. Hauert, C. Drouilly, D. Curulla-Ferre and J. Perez-Ramirez, *Angew. Chem., Int. Ed.*, 2016, **55**, 6261–6265.
86 T. Yan, L. Wang, Y. Liang, M. Makaremi, T. E. Wood, Y. Dai, B. Huang, F. M. Ali, Y. Dong and G. A. Ozin, *Nat. Commun.*, 2019, **10**, 2521.
87 F. Lei, Y. Sun, K. Liu, S. Gao, L. Liang, B. Pan and Y. Xie, *J. Am. Chem. Soc.*, 2014, **136**, 6826–6829.
88 Y. Li, X. Bai, D. Yuan, C. Yu, X. San, Y. Guo, L. Zhang and J. Ye, *Nat. Commun.*, 2023, **14**, 3171.

89 J. Ren, S. Ouyang, H. Xu, X. Meng, T. Wang, D. Wang and J. Ye, *Adv. Energy Mater.*, 2017, **7**, 1601657.
90 S. M. Meier-Menches, C. Gerner, W. Berger, C. G. Hartinger and B. K. Keppler, *Chem. Soc. Rev.*, 2018, **47**, 909–928.
91 G. Chen, R. Gao, Y. Zhao, Z. Li, G. I. N. Waterhouse, R. Shi, J. Zhao, M. Zhang, L. Shang, G. Sheng, X. Zhang, X. Wen, L. Z. Wu, C. H. Tung and T. Zhang, *Adv. Mater.*, 2018, **30**, 1704663.
92 R. Song, Z. Li, J. Guo, P. N. Duchesne, C. Qiu, C. Mao, J. Jia, S. Tang, Y. F. Xu, W. Zhou, L. Wang, W. Sun, X. Yan, L. Guo, D. Jing and G. A. Ozin, *Angew. Chem., Int. Ed.*, 2023, **62**, e202304470.
93 J. Zhu, W. Shao, X. Li, X. Jiao, J. Zhu, Y. Sun and Y. Xie, *J. Am. Chem. Soc.*, 2021, **143**, 18233–18241.
94 Y. Wang, E. Chen and J. Tang, *ACS Catal.*, 2022, **12**, 7300–7316.
95 W. H. Li, J. Yang and D. Wang, *Angew. Chem., Int. Ed.*, 2022, **61**, e202213318.
96 H. Ou, G. Li, W. Ren, B. Pan, G. Luo, Z. Hu, D. Wang and Y. Li, *J. Am. Chem. Soc.*, 2022, **144**, 22075–22082.
97 G. Wang, Z. Chen, T. Wang, D. Wang and J. Mao, *Angew. Chem., Int. Ed.*, 2022, **61**, e202210789.
98 L. Mascaretti, A. Schirato, T. Montini, A. Alabastri, A. Naldoni and P. Fornasiero, *Joule*, 2022, **6**, 1727–1732.
99 K. Yang, Z. Gu, Y. Long, S. Lin, C. Lu, X. Zhu, H. Wang and K. Li, *Green Energy Environ.*, 2021, **6**, 678–692.
100 P. Tang, Q. Zhu, Z. Wu and D. Ma, *Energy Environ. Sci.*, 2014, **7**, 2580–2591.
101 Y. Song, E. Ozdemir, S. Ramesh, A. Adishev, S. Subramanian, A. Harale, M. Albuali, B. A. Fadhel, A. Jamal, D. Moon, S. H. Choi and C. T. Yavuz, *Science*, 2020, **367**, 777–781.
102 O. Ola and M. M. Maroto-Valer, *J. Photochem. Photobiol., C*, 2015, **24**, 16–42.
103 B. Han, W. Wei, L. Chang, P. Cheng and Y. H. Hu, *ACS Catal.*, 2015, **6**, 494–497.
104 T. Xie, Z.-Y. Zhang, H.-Y. Zheng, K.-D. Xu, Z. Hu and Y. Lei, *Chem. Eng. J.*, 2022, **429**, 132507.
105 Z. Zhu, W. Guo, Y. Zhang, C. Pan, J. Xu, Y. Zhu and Y. Lou, *Carbon Energy*, 2021, **3**, 519–540.
106 Q. Li, H. Wang, M. Zhang, G. Li, J. Chen and H. Jia, *Angew. Chem., Int. Ed.*, 2023, **62**, e202300129.
107 Q. Hu, Y. Li, J. Wu, Y. Hu, H. Cao and Y. Yang, *Adv. Energy Mater.*, 2023, **13**, 2300071.
108 Y. Yao, B. Li, X. Gao, Y. Yang, J. Yu, J. Lei, Q. Li, X. Meng, L. Chen and D. Xu, *Adv. Mater.*, 2023, **35**, e2303654.
109 S. Shoji, X. Peng, A. Yamaguchi, R. Watanabe, C. Fukuhara, Y. Cho, T. Yamamoto, S. Matsumura, M.-W. Yu, S. Ishii, T. Fujita, H. Abe and M. Miyauchi, *Nat. Catal.*, 2020, **3**, 148–153.
110 W. Zhou, B. H. Wang, L. Tang, L. Chen, J. K. Guo, J. B. Pan, B. Lei, B. Hu, Z. J. Bai, M. Tulu, Z. X. Li, X. Wang, C. T. Au and S. F. Yin, *Adv. Funct. Mater.*, 2023, **33**, 2214068.
111 J. Zhao, X. Guo, R. Shi, G. I. N. Waterhouse, X. Zhang, Q. Dai and T. Zhang, *Adv. Funct. Mater.*, 2022, **32**, 2204056.
112 A. Tavasoli, A. Gouda, T. Zahringer, Y. F. Li, H. Quaid, C. J. Viasus Perez, R. Song, M. Sain and G. Ozin, *Nat. Commun.*, 2023, **14**, 1435.
113 J. Zhang, Y. Li, J. Sun, H. Chen, Y. Zhu, X. Zhao, L.-C. Zhang, S. Wang, H. Zhang, X. Duan, L. Shi, S. Zhang, P. Zhang, G. Shao, M. Wu, S. Wang and H. Sun, *Appl. Catal., B*, 2022, **309**, 121263.
114 Z. Rao, Y. Cao, Z. Huang, Z. Yin, W. Wan, M. Ma, Y. Wu, J. Wang, G. Yang, Y. Cui, Z. Gong and Y. Zhou, *ACS Catal.*, 2021, **11**, 4730–4738.
115 V. Smil, *Nature*, 1999, **400**, 415.
116 J. W. Erisman, M. A. Sutton, J. Galloway, Z. Klimont and W. Winiwarter, *Nat. Geosci.*, 2008, **1**, 636–639.
117 D. Mateo, A. Sousa, M. Zakharzhevskii and J. Gascon, *Green Chem.*, 2024, **26**, 1041–1061.
118 C. Hu, X. Chen, J. Jin, Y. Han, S. Chen, H. Ju, J. Cai, Y. Qiu, C. Gao, C. Wang, Z. Qi, R. Long, L. Song, Z. Liu and Y. Xiong, *J. Am. Chem. Soc.*, 2019, **141**, 7807–7814.
119 L. W. Chen, Y. C. Hao, Y. Guo, Q. Zhang, J. Li, W. Y. Gao, L. Ren, X. Su, L. Hu, N. Zhang, S. Li, X. Feng, L. Gu, Y. W. Zhang, A. X. Yin and B. Wang, *J. Am. Chem. Soc.*, 2021, **143**, 5727–5736.
120 T. Hou, L. Chen, Y. Xin, W. Zhu, C. Zhang, W. Zhang, S. Liang and L. Wang, *ACS Energy Lett.*, 2020, **5**, 2444–2451.
121 H. Bai, S. H. Lam, J. Yang, X. Cheng, S. Li, R. Jiang, L. Shao and J. Wang, *Adv. Mater.*, 2022, **34**, e2104226.
122 S. Wang, W. Yu, S. Xu, K. Han and F. Wang, *ACS Sustainable Chem. Eng.*, 2021, **10**, 115–123.
123 X. Li, X. Zhang, H. O. Everitt and J. Liu, *Nano Lett.*, 2019, **19**, 1706–1711.
124 Y. Peng, J. Albero, A. Franconetti, P. Concepcion and H. Garcia, *ACS Catal.*, 2022, **12**, 4938–4946.
125 X. Bian, Y. Zhao, G. I. N. Waterhouse, Y. Miao, C. Zhou, L. Z. Wu and T. Zhang, *Angew. Chem., Int. Ed.*, 2023, **62**, e202304452.
126 S. Lee, Y. R. Lee, S. J. Kim, J.-S. Lee and K. Min, *Chem. Eng. J.*, 2023, **454**, 140470.
127 C. Xing, H. Cai, D. Kang and W. Sun, *Adv. Energy Sustainability Res.*, 2023, **4**, 2300015.
128 Y. Li, Q. Guan, G. Huang, D. Yuan, F. Xie, K. Li, Z. Zhang, X. San and J. Ye, *Adv. Energy Mater.*, 2022, **12**, 2202459.
129 H. Ge, Y. Kuwahara, K. Kusu, Z. Bian and H. Yamashita, *Appl. Catal., B*, 2022, **317**, 121734.
130 Y. Wang, A. Zavabeti, F. Haque, B. Y. Zhang, Q. Yao, L. Chen, D. Chen, Y. Hu, N. Pillai, Y. Liu, K. A. Messalea, C. Yang, B. Jia, D. M. Cahill, Y. Li, C. F. McConville, J. Z. Ou, L. Kong, X. Wen and W. Yang, *Mater. Today*, 2022, **55**, 21–28.
131 G. Firestone, H. Huang, J. R. Bochinski and L. I. Clarke, *Nanotechnology*, 2019, **30**, 475706.
132 H. Huang, G. Firestone, D. Fontecha, R. E. Gorga, J. R. Bochinski and L. I. Clarke, *Nanoscale*, 2020, **12**, 904–923.
133 Y. Liu, Q. Zhong, P. Xu, H. Huang, F. Yang, M. Cao, L. He, Q. Zhang and J. Chen, *Matter*, 2022, **5**, 1305–1317.
134 Y. Liu, X. Wang, Q. Li, T. Yan, X. Lou, C. Zhang, M. Cao, L. Zhang, T. K. Sham, Q. Zhang, L. He and J. Chen, *Adv. Funct. Mater.*, 2022, **33**, 2210283.
135 Y. Liu, C. Li, H. Yu and J. Guo, *Chem*, 2022, **8**, 2586–2588.

136 R. Cao, M. Q. Zhang, C. Hu, D. Xiao, M. Wang and D. Ma, *Nat. Commun.*, 2022, **13**, 4809.
137 Y. Liu, C. Zhang, J. Feng, X. Wang, Z. Ding, L. He, Q. Zhang, J. Chen and Y. Yin, *Angew. Chem., Int. Ed.*, 2023, **62**, e202308930.
138 H. Luo, D. Yao, K. Zeng, J. Li, S. Yan, D. Zhong, J. Hu, H. Yang and H. Chen, *Fuel Process. Technol.*, 2022, **230**, 107205.
139 Y. Miao, Y. Zhao, G. I. N. Waterhouse, R. Shi, L. Z. Wu and T. Zhang, *Nat. Commun.*, 2023, **14**, 4242.
140 M. Bonn, S. Funk, Ch Hess, N. D. Denzler and C. Stampfl, *Science*, 1999, **285**, 1042–1045.
141 E. Hansjosten, A. Wenka, A. Hensel, W. Benzinger, M. Klumpp and R. Dittmeyer, *Chem. Eng. Process.*, 2018, **130**, 119–126.
142 S. Zoller, E. Koepf, D. Nizamian, M. Stephan, A. Patane, P. Haueter, M. Romero, J. Gonzalez-Aguilar, D. Lieftink, E. de Wit, S. Brendelberger, A. Sizmann and A. Steinfeld, *Joule*, 2022, **6**, 1606–1616.
143 X. Ding, Z. Zhang, J. Sun, J. Y. Y. Loh, D. Ji, J. Lu, C. Liu, L. Zhao, W. Liu, J. Zhao, S. Tang, M. Safari, H. Cai, W. Tu, N. P. Kherani, Z. Hu, G. A. Ozin, Z. Zou and L. Wang, *Joule*, 2023, **7**, 2318–2334.

